

See discussions, stats, and author profiles for this publication at: <https://www.researchgate.net/publication/248790527>

Compression-Induced Microcrack Growth in Brittle Solids: Axial Splitting and Shear Failure

Article in *Journal of Geophysical Research Atmospheres* · January 1985

DOI: 10.1029/JB090iB04p03105

CITATIONS

560

READS

1,201

2 authors:



Hideyuki Horii

The University of Tokyo

117 PUBLICATIONS 3,228 CITATIONS

SEE PROFILE



S. Nemat-Nasser

University of California, San Diego

537 PUBLICATIONS 24,368 CITATIONS

SEE PROFILE

Some of the authors of this publication are also working on these related projects:



1. Phononic and photonics crystals [View project](#)



Micromechanics-Based Continuum Analysis [View project](#)

Compression-Induced Microcrack Growth in Brittle Solids: Axial Splitting and Shear Failure

H. HORII AND S. NEMAT-NASSER

*Department of Civil Engineering, The Technological Institute, Northwestern University
Evanston, Illinois*

Micromechanisms of rock failure (axial splitting and shear failure) are examined in light of simple mathematical models motivated by microscopic observations. The elasticity boundary value problem associated with cracks growing from the tips of a model flaw is solved. It is shown that under axial compression, tension cracks nucleate at the tips of the preexisting model flaw, grow with increasing compression, and become parallel to the direction of the maximum far-field compression. When a lateral compression also exists, the crack growth is stable and stops at some finite crack length. With a small lateral tension, on the other hand, the crack growth becomes unstable after a certain crack length is attained. This is considered to be the fundamental mechanism of axial splitting observed in uniaxially compressed rock specimens. To model the mechanism of shear failure, a row of suitably oriented model flaws is considered and the elasticity boundary value problem associated with the out-of-plane crack growth from the tips of the flaws is solved. It is shown that for a certain overall orientation of the flaws the growth of the out-of-plane cracks may become unstable, leading to possible macroscopic faulting. On the basis of this model the variations of the "ultimate strength" and the orientation of the overall fault plane with confining pressure are estimated, and the results are compared with published experimental data. In addition, the results of a set of model experiments on plates of Columbia resin CR39 containing preexisting flaws are reported. These experiments are specifically designed in order to show the effect of confining pressure on the crack growth regime. The experiments seem to support qualitatively the analytical results.

1. INTRODUCTION

Brittle solids such as rocks, by their nature, contain numerous flaws, cavities, inclusions, and other inhomogeneities. Materials of this kind fail under axial compression by axial splitting when the confining pressure is zero or very small and by faulting or (macroscopic) shear failure when the confining pressure is moderate but still below the brittle-ductile transition value. The strength, the orientation of the macroscopic failure plane, the dilatancy, and other mechanical features are greatly affected by the confining pressure. Nucleation, growth, and interaction of microcracks are considered to be the dominant, controlling micromechanisms of macroscopic failure; see, for example, Paterson [1958, 1978], Griggs and Handin [1960], Brace [1964], Gramberg [1965], Fairhurst and Cook [1966], Mogi [1966], Scholz [1968], Friedman *et al.* [1970], Hoshino and Koide [1970], Wawersik and Brace [1971], Peng and Johnson [1972], Hallbauer *et al.* [1973], Olsson and Peng [1976], Tapponnier and Brace [1976], Holzhausen [1978], Holzhausen and Johnson [1979], Wong [1982a, b], and Kranz [1983]. For reviews and references, see Paterson [1978] and Kranz [1983].

Models of microcracking have been postulated based on the idea that frictional sliding along preexisting cracks results in the formation of tension cracks at the tips of the preexisting cracks, and experiments on glass and photoelastic plates have been performed to illustrate this process [Brace and Bombolakis, 1963; Hoek and Bieniawski, 1965; Bombolakis, 1968]. In addition, model calculations have been made in order to quantify the microfracturing and the associated dilatancy and other macroscopic manifestations [McClintock and Walsh, 1963; Holcomb, 1978; Ingraffea and Heuze, 1980; Dey and Wang, 1981; Kachanov, 1982a, b; Moss and Gupta, 1982; Nemat-Nasser and Horii, 1982].

Copyright 1985 by the American Geophysical Union.

Paper number 4B5089.
0148-0227/85/004B-5089\$05.00

Since about 1970, the use of high-resolution scanning electron microscopes has produced a considerable amount of information on the sources of microcracks and their growth in response to applied loads [Brace *et al.*, 1972; Sprunt and Brace, 1974; Dengler, 1976; Tapponnier and Brace, 1976; Kranz, 1979; Wong, 1982b]. It has been observed that isolated preexisting, Griffith-type cracks are seldom seen to be the major source of microcracking, and many sources (or stress concentrators), other than the preexisting cracks, have been identified. In Westerly granite, for example, Tapponnier and Brace [1976] report that sets of grain boundary, low-aspect ratio cavities, as well as suitably oriented interfaces of two different minerals (biotite often being involved), produce most of the microcracks. For marble, Olsson and Peng [1976] observe, with the aid of optical microscopy, cracks forming at the intersections of inclined (relative to maximum axial compression) lamellae (or slip bands [Cottrell, 1953]) and grain boundaries. More recently, Wong [1982b] has made a detailed microscopic observation of the fracture process in Westerly granite at high pressures and temperatures. Wong confirms many early observations. In addition, he reports for prefailure loadings the presence of microcracks at high angles (15° – 45°) relative to the axial compression, which can slip by overcoming the frictional resistance along their surfaces.

It is essential that the development of analytic models for microcracking be guided by these physical observations. A model of this kind is considered in section 2, and its relation to the microscopically observed deformation processes is discussed. It is concluded that although preexisting, frictional microcracks are seldom observed to be the source of microcracking, the shear crack model proposed by Brace and Bombolakis [1963] still presents a reasonable idealization, if it is properly interpreted as a "microflaw" associated, for example, with a set of grain boundary cavities, a soft inclusion, a cleavage, a slip band, or even with a high-angle frictional crack. A microflaw of this kind may have frictional resistance, cohesive shear resistance (due to its in-plane plastic deformation), or

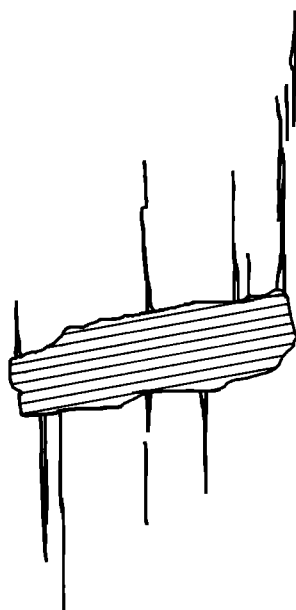


Fig. 1a

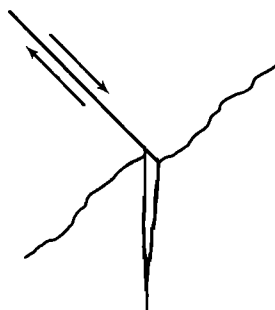


Fig. 1b

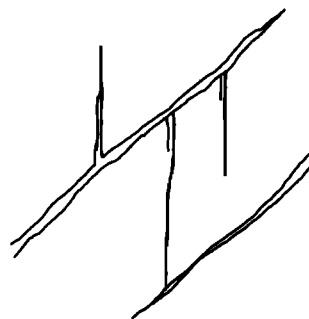


Fig. 1c

Fig. 1. Sketch of stress-induced microcracks (a) at a biotite grain boundary, (b) at the intersection of an inclined lamella and a grain boundary, and (c) at preexisting grain boundary cavities. Figures 1a and 1c are in Westerly granite [from *Tapponnier and Brace*, 1976], and Figure 1b is in Tennessee marble [from *Olsson and Peng*, 1976].

both, depending on which actual mechanism it may be approximating. In the present work we use this model flaw as a basic source for microcracking and assume that it represents adequately the effects of actual flaws.

In section 2 a mathematical model of curved crack growth from the tips of a model "microflaw" is defined as a two-dimensional, elasticity boundary value problem. The exact formulation of this boundary value problem is given, and numerical results for curved crack growth are obtained. (The problem of noncoplanar crack growth under far-field tension (but not compression) has been extensively dealt with in the literature; see, for example, *Banichuk* [1970], *Lo* [1978], *Palaniswamy and Knauss* [1978], *Wu* [1978], *Cotterell and Rice* [1980], *Nemat-Nasser* [1980], *Hayashi and Nemat-Nasser* [1981], and *Karihaloo* [1982] for a review). Crack paths, crack extension lengths, and their relation to the applied overall loads are established, using an incremental approach; this is a considerable improvement on our previous calculations which were based on a straight crack path [*Nemat-Nasser and Horii*, 1982]. It is shown that in the presence of some (very small) far-field lateral tension the growth process of cracks emanating from the tips of a model flaw in an extended solid becomes unstable after a certain length is attained, with the cracks growing spontaneously in the direction of maximum axial compression. The phenomenon of axial splitting is discussed in terms of this model.

Another aspect of brittle failure relates to the distribution of microcracks within the sample and to the evolution of this distribution as the peak axial load is approached. Here, a great deal has been learned by the use of optical microscopy, acoustic emission, scanning electron microscopy, and other methods; see, for example, *Scholz* [1968], *Hoshino and Koide* [1970], *Hallbauer et al.* [1973], *Liu and Livanos* [1976], *Soga et al.* [1976], *Lockner and Byerlee* [1977], and *Wong* [1982b]. It is reported that as the axial load is increased, the growth of microcracks accelerates, leading to the formation of regions of high crack density in a narrow zone which eventually becomes

a macroscopic shear fracture plane. This localized, high microcrack density zone materializes when the magnitude of the applied axial compression is close to the ultimate strength of the specimen. (It should be pointed out, however, that some experimental observations seem to suggest the initiation of localized deformations at rather low stresses; see, for example, *Soga et al.* [1978].) Most of the microcracks are in the axial direction; see *Friedman et al.* [1970], *Wawersik and Brace* [1971], *Dunn et al.* [1973], *Hallbauer et al.* [1973], *Olsson and Peng* [1976], *Tapponnier and Brace* [1976], and *Wong* [1982b] for discussions and references.

In section 3 we consider a mathematical model for simulating microscopic events which may be instrumental in the inception of macroscopic shear failure. The model consists of a row of "microflaws" in an infinitely extended, linearly elastic, two-dimensional solid under far-field lateral, as well as axial, compression. (From the mathematical point of view, this represents a rather difficult problem in two-dimensional elasticity, which has not been dealt with before. In this paper, we outline a powerful technique for solving this and other similar problems involving interacting flaws or inhomogeneities. We note that problems of this kind also occur in many geological formations; see, for example, *Segall and Pollard* [1980], *Pollard et al.* [1982], and *Deng and Zhang* [1984].) It is shown that because of interaction, the growth regime of cracks emanating from the tips of the flaws may suddenly become unstable at a certain axial load, with cracks growing spontaneously in the direction of maximum axial compression. For this mathematical model we define the smallest axial stress at instability as the ultimate strength and the associated overall orientation of the row of flaws as the fault orientation. In this manner, the variation of the ultimate strength and the orientation of the overall fault plane with confining pressure are estimated, and the results are compared with some published experimental data.

In addition, we report the results of a set of relevant "model experiments" which are specifically designed to test the effect

of the confining pressure on the crack growth regime. The models consist of thin plates of Columbia resin CR39, containing preexisting, straight, thin flaws of different sizes. It is shown that, in the absence of lateral confinement, cracks emanating from the tips of large and compliant flaws grow under axial compression in the axial direction, leading to axial splitting. On the other hand, the presence of confining pressure arrests crack growth of this kind. However, at a certain stage of loading, cracks emanating from the tips of sets of smaller, less compliant flaws suddenly grow in an unstable manner, forming a localized cracked zone.

2. AXIAL SPLITTING

Under axial compression, microcracks may nucleate at boundaries of suitably oriented, preexisting microflaws and grow in the direction of the axial load. A flaw may be a preexisting, soft inhomogeneity, such as biotite in granite (Figure 1a) or a slip band or lamella in a plastically deformed grain of marble (Figure 1b), or it may be a connected set of low-aspect ratio grain boundary cavities (Figure 1c) [Olsson and Peng, 1976; Tapponnier and Brace, 1976; Wong, 1982b]. From the mechanics point of view, any material or geometric discontinuity may serve as a stress concentrator and may hence promote crack nucleation and crack growth. For example, Brace and Bombolakis [1963] and Hoek and Bieniawski [1965] have shown that a suitably oriented, Griffith-type, preexisting crack in a glass plate can grow out of its own plane when the plate is compressed axially. In this case, tension cracks are nucleated at the tips of the preexisting crack because of the relative sliding of the faces of the preexisting crack. Nemat-Nasser and Horii [1982], on the other hand, use a thin (6 mm) plate of Columbia resin CR39, containing a small slit (instead of a crack) of about 0.4 mm width, fitted with two 0.2-mm-thick brass sheets, and they show that a similar crack nucleation and growth is observed under axial compression. Typical examples are shown in Figures 2 and 3. (In fact, a similar crack nucleation and growth regime results if an inclusion is embedded and glued to the plate [see Nemat-Nasser, 1983, p. 186, Figures 3 and 4].)

2.1. A Model for "Flaws"

From the above comments and based on physical observations reported in the literature, as discussed in section 1, it is clear that there are numerous complex mechanisms which may be responsible for microcracking in an actual rock specimen. To produce an analytically manageable model of a microflaw, a drastic idealization is necessary. The microscopic observations seem to suggest that one of the major mechanisms of microcrack nucleation and growth is the shear deformation due to glide (plastic flow), or slip along the lamellae, or possibly due to the frictional sliding along the interface cavities or cleavage cracks. The simplest reasonable model which represents such mechanisms is a line discontinuity, a "microflaw," PP' in Figure 4, which can glide in its own plane, having a glide or shear resistance of magnitude $\tau_c + \mu|\sigma_y|$, where τ_c is the cohesive yield stress, μ is an average friction coefficient, and σ_y is the (variable) compressive force transmitted across the flaw; σ_y is a function of x . In general, τ_c may depend on the strain history of the flaw material, but for simplicity it may be taken to be a constant; this corresponds to perfect plasticity. When $\mu \ll 1$, the frictional resistance is small and the flaw is akin to a thin plastic inclusion which can flow under shear stress τ_c . On the other hand, when $\tau_c \ll \mu|\sigma_y|$,

the flaw resembles a crack with frictional resistance. In either case, the qualitative results turn out to be the same: under axial compression, tension cracks are nucleated at the tips of the flaw at about a 70° angle with respect to the flaw direction. These cracks grow in a stable manner, curving toward the direction of axial compression.

The two-dimensional, elasticity boundary value problem associated with the idealized microflaw PP' and with the corresponding curved cracks PQ and P'Q' (Figure 4) satisfies the following conditions:

$$u_y^+ = u_y^- \quad \tau_{xy}^+ = \tau_{xy}^- = -\tau_c + \mu\sigma_y \quad \text{on PP'}$$

and

$$\sigma_\theta = \tau_{r\theta} = 0 \quad \text{on PQ and P'Q'}$$

where u_y is the displacement in the y direction, τ_{xy} is the shear stress and σ_y is the normal stress on PP', σ_θ is the hoop stress, $\tau_{r\theta}$ is the shear stress in polar coordinates on the extended crack PQ, the superscript plus denotes the value of the involved quantity on the positive face (defined by the positive y direction) of the flaw, and the superscript minus is the value on the other side. The exact formulation of this boundary value problem is presented in Appendix A. On the basis of this formulation the curved crack path is calculated incrementally, and the corresponding crack length is obtained as a function of the applied load.

Before discussing these results, it may be of some interest to examine the relative influence of plastic glide and frictional sliding of the preexisting flaw, PP', on the crack growth process. To this end we have used the straight out-of-plane crack profile and, following the method of solution given by Nemat-Nasser and Horii [1982], have obtained the normalized axial compression, $|\sigma_1|(\pi c)^{1/2}/K_{Ic}$, as a function of the normalized crack length, l/c , for $\sigma_2/\sigma_1 = -0.08$ and different values of τ_c and μ ; K_{Ic} is the mode I fracture toughness of the matrix material, σ_1 is the axial stress, σ_2 is the lateral stress (tension is regarded positive), and c is half the length of the preexisting mathematical flaw. Typical results are presented in Figure 5. It is seen that a flaw which can only glide plastically with no friction ($\tau_c \neq 0$, $\mu = 0$) produces essentially the same qualitative result as a flaw which can undergo frictional sliding with no plastic resistance ($\mu \neq 0$, $\tau_c = 0$). Indeed, as pointed out at the beginning of this section, the presence of any kind of flaw, even a "rigid" inclusion, would result in a similar out-of-plane crack growth under axial compression.

Figure 6 shows the crack profiles for $\tau_c = 0$, calculated incrementally, and compares these with experimentally observed ones as well as with those calculated approximately by Nemat-Nasser and Horii [1982]. It is seen that the present solution method yields results that compare better with experimental observations.

2.2. Effect of Confinement on Crack Growth

The most significant result which emerged from the analytical calculations is the effect of lateral stress on the crack growth process. Figure 7 shows typical axial load versus extended curved crack length relations (incrementally obtained using the formulation of Appendix A) for $\tau_c = 0$, indicated lateral tensions ($\sigma_2/\sigma_1 < 0$), and lateral compressions ($\sigma_2/\sigma_1 > 0$). As is seen, the presence of slight lateral tension renders the out-of-plane, curved crack growth unstable in the sense that after a suitable critical length is attained, the crack grows spontaneously and without an increase in axial compression,

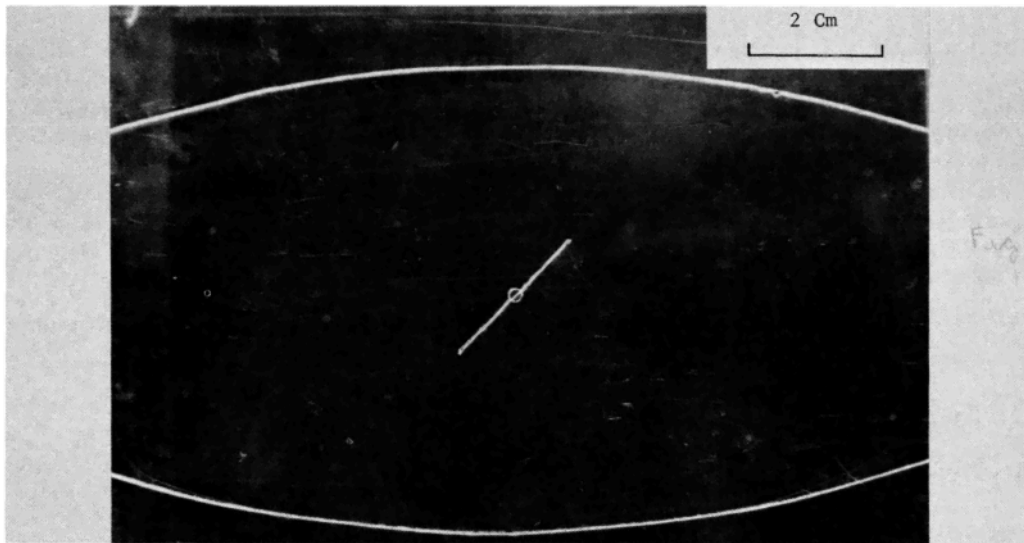


Fig. 2a

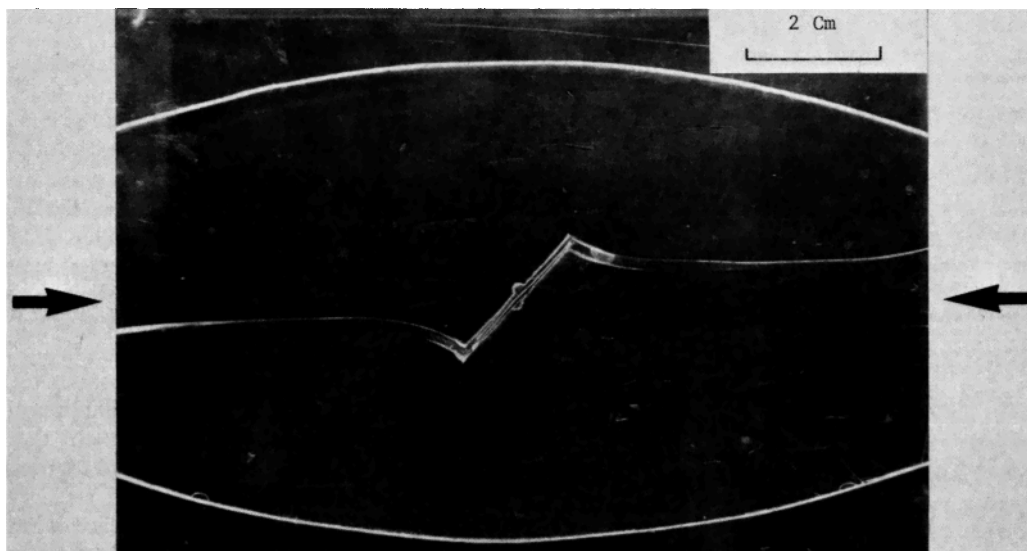


Fig. 2b

Fig. 2. (a) A barrel-shaped model specimen containing a preexisting flaw. (b) Unstable crack growth under axial compression.

leading to the splitting of the specimen. On the other hand, if far-field lateral compression is present, then no such unstable growth is observed. Indeed, if the far-field lateral compression is a small percentage of the far-field axial compression, then the out-of-plane, curved (tension) crack attains a finite length and does not grow any further.

Model experiments support these results. Figure 2 shows crack nucleation and growth under axial compression in a barrel-shaped specimen which initially contains a slit (of 0.4 mm width) filled with two thin brass sheets (of 0.2 mm thickness). In this case, a slight lateral tension exists because of the geometry of the specimen, and thus out-of-plane crack extension is unstable. Figure 3 shows a dogbone-shaped specimen,

where lateral compression accompanies the axial one. In this case, the crack growth is stable.

Since the ordinate in Figure 7 (and also in Figure 5) is $|\sigma_1|(\pi c)^{1/2}/K_c$, it is seen that for a given extension length l/c , the corresponding axial compression σ_1 is inversely proportional to $c^{1/2}$. Therefore, in a specimen which includes several isolated, preexisting flaws of various lengths, over a rather wide range of flaw orientations the large (and consequently more compliant) flaws nucleate microcracks first. If some lateral tension exists or is produced as a consequence of end constraint, the finiteness of the sample, the sample geometry (e.g., Figure 2), or the presence of other inhomogeneities, or, in fact, as a consequence of the crack growth itself, then cracks

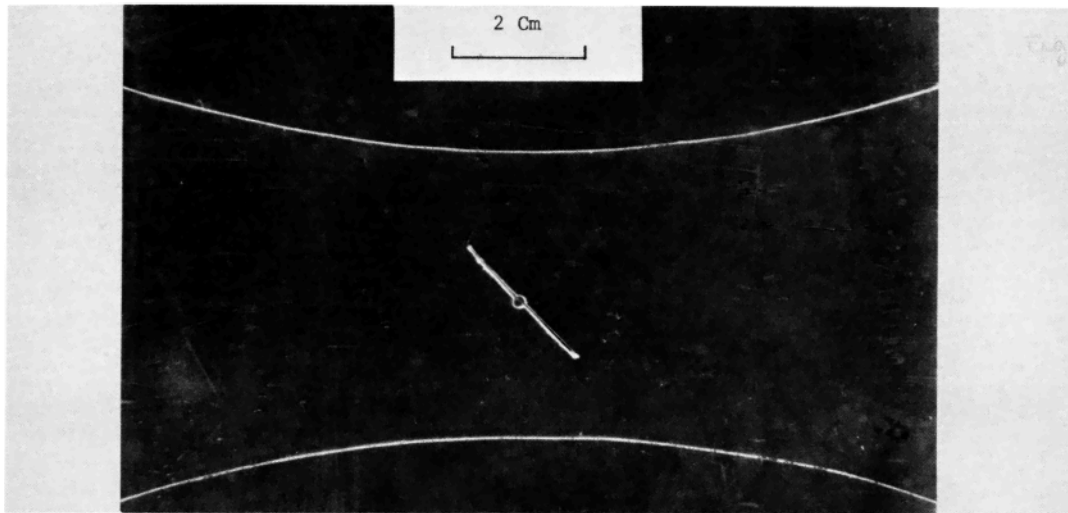


Fig. 3a

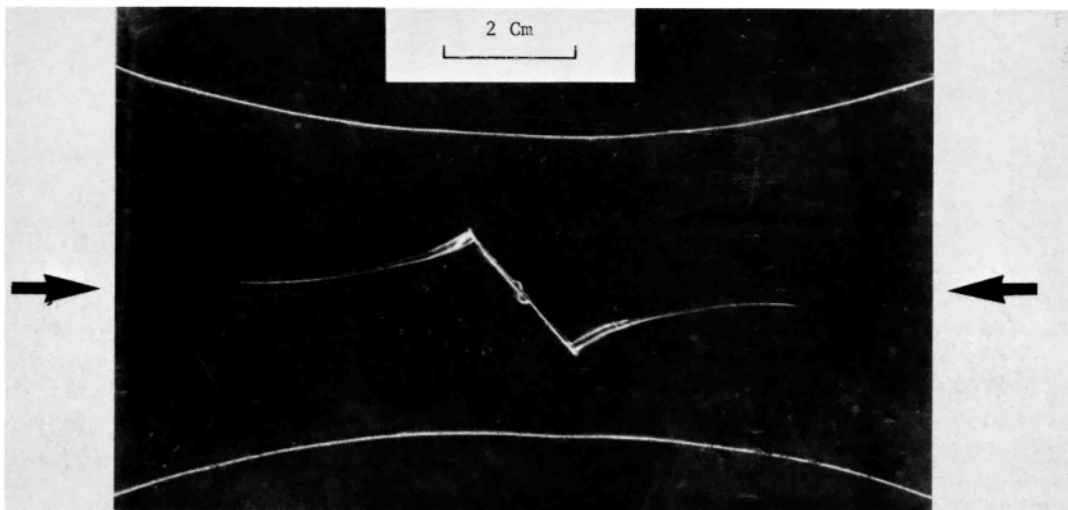


Fig. 3b

Fig. 3. (a) A dogbone-shaped model specimen containing a preexisting flaw. (b) Stable crack growth under axial compression.

would extend from the large flaws in an unstable manner, joining each other and leading to axial splitting.

Figure 20 of *Nemat-Nasser and Horii* [1982, p. 6819] is a model illustration of such a splitting process. However, the most dramatic example is given in Figure 8. Here, the model specimen contains a number of large, preexisting, brass-fitted slits or flaws and a row of suitably arranged, smaller, similar flaws (Figure 8a). Upon axial compression, the larger flaws nucleate cracks first. These cracks grow (Figures 8b and 8c), and finally lead to axial splitting (Figure 8c) and actual shattering of the specimen (Figure 8d), while many of the small flaws have not even nucleated any cracks.

The situation is changed completely when lateral pressure is also present. Figure 9 shows the growth regime of the cracks in a sample with essentially the same preexisting flaws but

with some lateral compression acting on the specimen. Here again, first large flaws nucleate cracks (Figure 9b). However, these cracks are soon arrested, and at a certain stage, some of the smaller flaws (Figure 9c) suddenly nucleate cracks. Immediately after this, and without an increase in the axial load, the entire row of the smaller flaws suddenly and spontaneously produces tension cracks (Figure 9d), which grow, curving toward the maximum compression direction and leading to "macroscopic" shear failure upon further loading (Figure 9e). These model experiments (Figures 8 and 9) clearly show the dramatic influence of the lateral pressure on the crack nucleation and growth process. The calculation for the optimal orientation and other aspects of the faulting process is discussed in the following section, where the results of additional model experiments are also given.

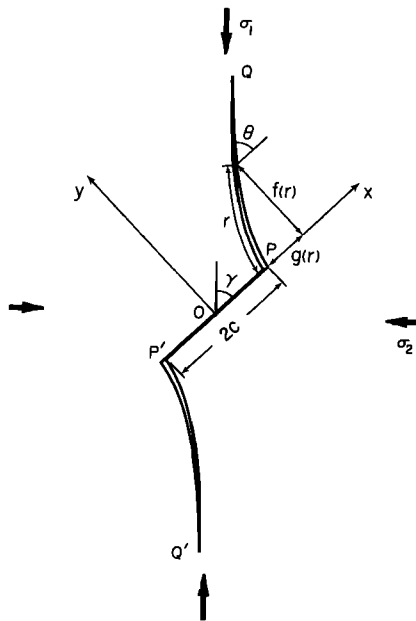


Fig. 4. Preexisting flaw P'P and curved cracks PQ and P'Q'.

As is pointed out in Appendix A, equation (8) of *Nemat-Nasser and Horii* [1982] involves an algebraic error which, although it does not affect the qualitative results discussed by the authors, does change the numerical results for large values of l/c . Since these authors use the numerical results of their Figure 9 to explain axial failure observed by *Peng and Johnson* [1972] for samples of Chelmsford granite with different inserts, it is appropriate to make some comments here.

Peng and Johnson report the following data for Chelmsford granite: the average initial flaw length $2c = 0.025$ in. (0.64 mm), the fracture toughness $K_c = 500$ psi in.^{1/2} (17.4 MPa mm^{1/2}), tensile strength $T = 1200$ psi (83 MPa), and compressive strength $C = 24,000$ psi (165 MPa) for the steel disk insert, 18,500 psi (127 MPa) for the teflon insert, and 15,000 psi (103 MPa) for the neoprene insert.

From the relation $K_c = T(\pi c)^{1/2}$, the effective initial flaw length for tensile fracture is $2c = 0.11$ in. (2.8 mm). Using this value, *Nemat-Nasser and Horii* [1982] report the normalized compressive strength, $C(\pi c)^{1/2}/K_c$, to be 20 for the steel disk insert, 15.4 for the teflon insert, and 12.5 for the neoprene insert. They plot these values in their Figure 9.

On the other hand, if we recognize that the fracture occurs under overall compressive force and is different from that

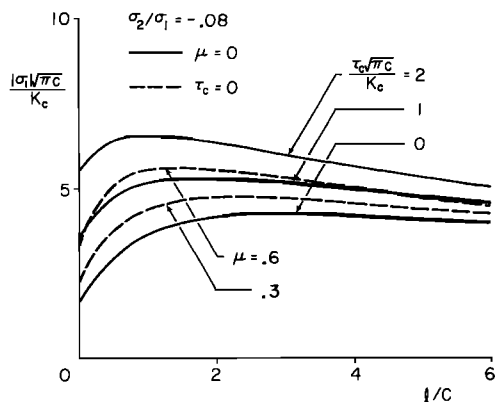
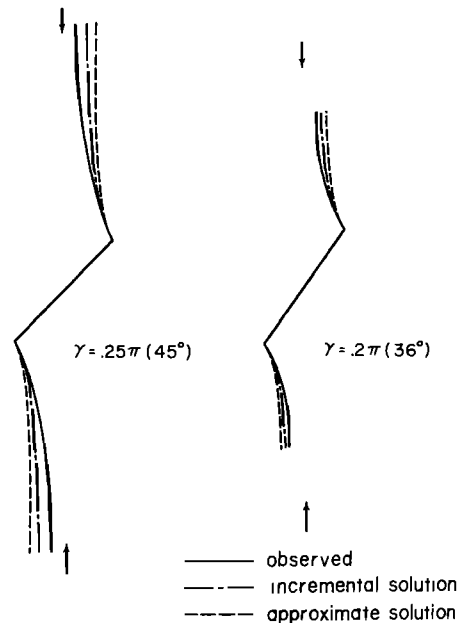
Fig. 5. Compressive force required to attain the associated crack length for indicated values of τ_c and μ ; straight crack calculation.

Fig. 6. Calculated and observed crack profiles.

under tensile force and if we therefore use the reported, observed initial flaw length, $2c = 0.025$ (0.64 mm), the normalized compressive strength, $C(\pi c)^{1/2}/K_c$, becomes 9.5 for the steel insert, 7.3 for the teflon insert, and 5.9 for the neoprene insert. These values seem to agree well with the numerical results of Figure 7 of this paper; note that these numerical results are obtained incrementally for curved crack growth, using the exact elasticity formulation of Appendix A. Indeed, *Peng* [1971] reports radial tensile stress of 6–8% of applied compression for the neoprene insert and 4–6% for the teflon insert.

Nemat-Nasser and Horii [1982] also use the numerical results of their Figure 9 to estimate the order of magnitude of tectonic stresses required to cause exfoliation. The more accurate results of Figure 7 of this paper do not, however, affect such order-of-magnitude estimates, although they tend to suggest smaller, necessary tectonic forces.

3. SHEAR FAILURE

On the basis of the observations of *Hoshino and Koide* [1970], *Hallbauer et al.* [1973], *Olsson and Peng* [1976],

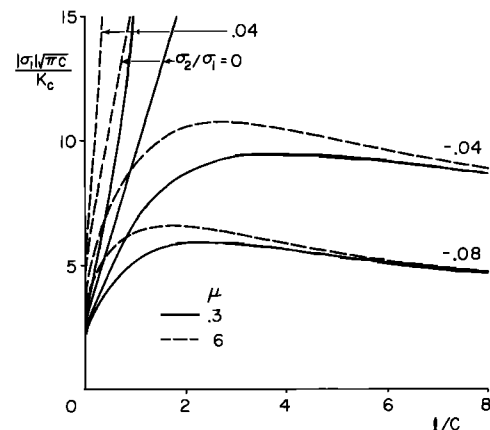


Fig. 7. Compressive force required to attain the associated crack length.



Fig. 8a

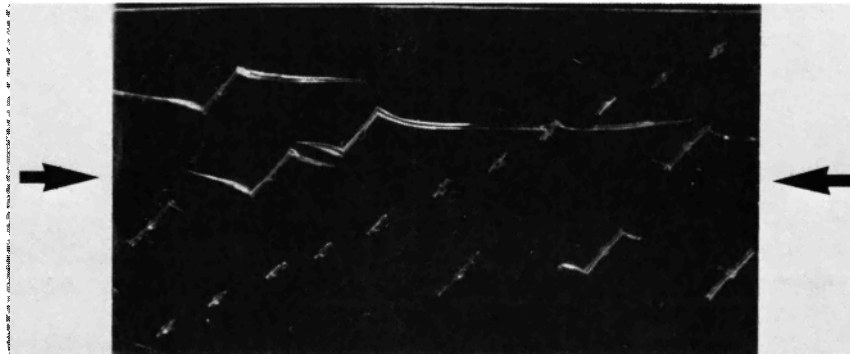


Fig. 8b

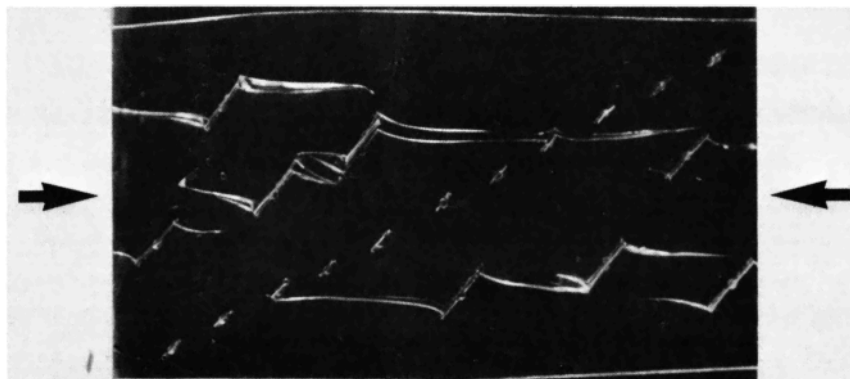


Fig. 8c

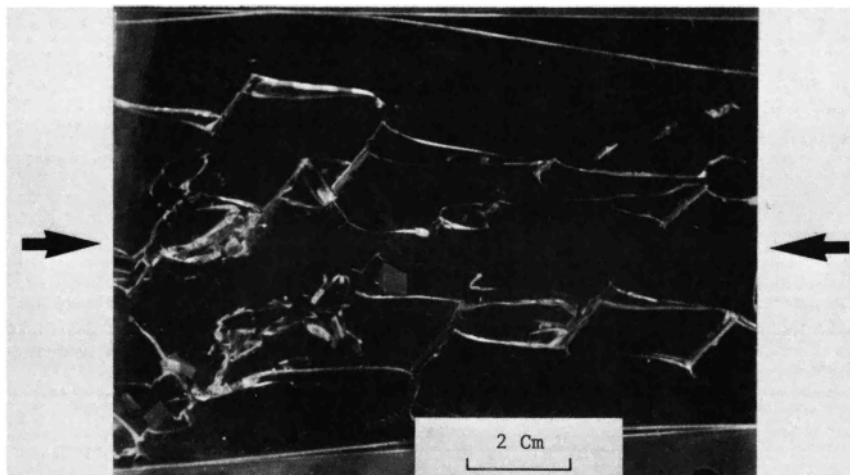


Fig. 8d

Fig. 8. (a) Specimen containing a row of small flaws and several larger flaws. (b) Under axial compression without confinement, cracks being nucleated first at larger flaws. (c) Axial splitting by the growth of cracks at larger flaws. (d) Shattering of the specimen while some smaller flaws are still inactive.



Fig. 9a

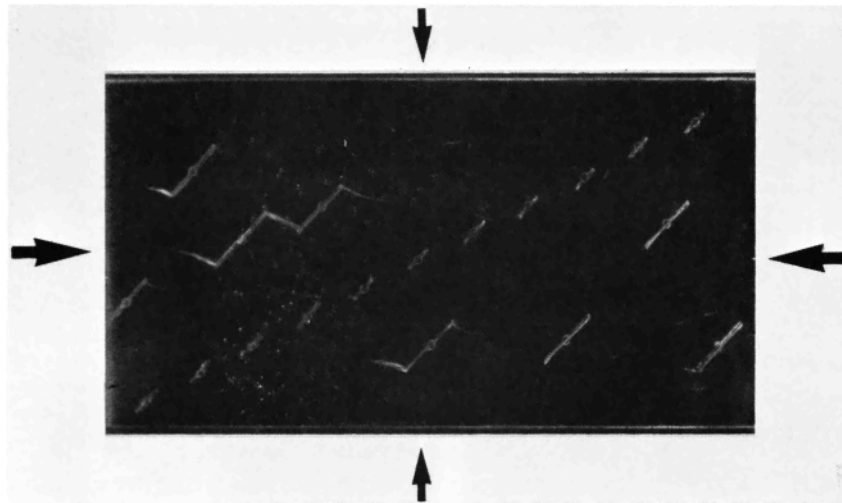


Fig. 9b

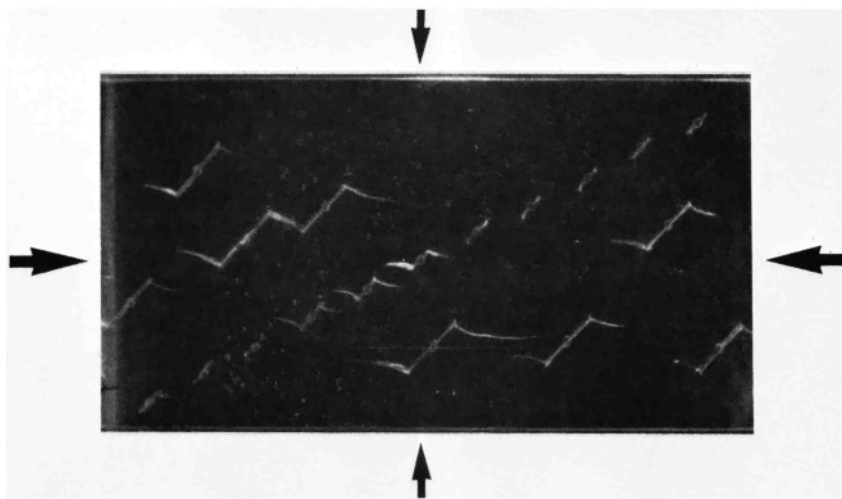


Fig. 9c

Fig. 9. (a) Specimen containing a row of small flaws and several larger flaws (same as in Figure 8a). (b) Under axial compression with confinement, cracks being nucleated first at larger flaws. (c) Cracks at larger flaws arrested because of confinement, and several smaller flaws just activated. (d) Without an increase in axial load, cracks growing suddenly at the entire row of smaller flaws. (e) Fault formation due to interactive growth of cracks at smaller flaws.

Lockner and Byerlee [1977], and our own model studies, it appears that shear failure may be modeled to be the result of unstable growth of cracks from suitably oriented sets of small, closely spaced, interacting flaws. Indeed, *Hallbauer et al.*, *Olsson and Peng*, *Lockner and Byerlee*, and others [see *Pater-*

son, 1978] report a nearly uniform distribution of crack density in rock specimens compressed axially under confining pressure, up to axial loads close to their maximum values. (As pointed out before, this does not seem to be a universally accepted experimental conclusion; see, for example, *Soga et al.*

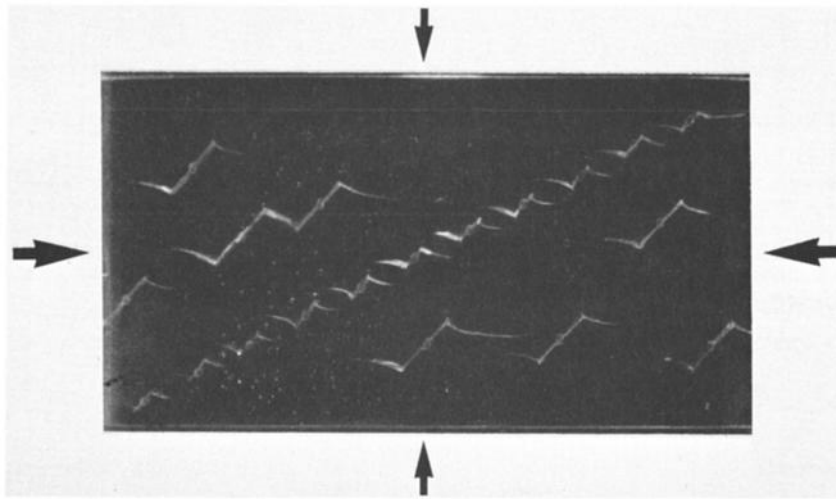


Fig. 9d

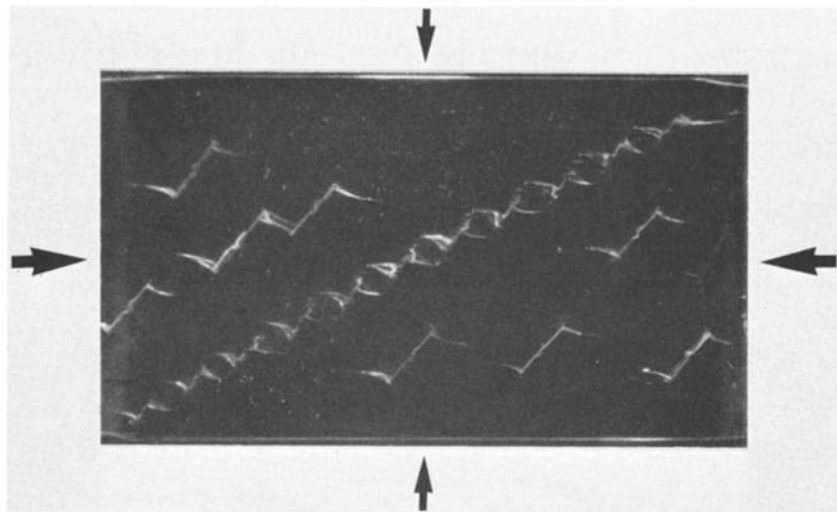


Fig. 9e

Fig. 9. (continued)

[1978], who report initiation of localized deformations at axial stresses of about 60% of the ultimate one.) These authors observe that for axial compressions close to the ultimate strength, a region of high crack density begins to emerge rapidly. Moreover, in this high-density crack zone the orientation of cracks is almost parallel to the axial compression, implying that these are tension cracks, nucleated and grown from various flaws. The high-density crack zone eventually produces the macroscopic shear failure plane.

3.1. A Model for Shear Failure

It appears that one essential feature of shear failure is the interaction of smaller flaws, which leads to the unstable growth of tension cracks. To capture this feature, we consider a row of equally spaced model flaws of equal initial size and of common orientation. (Even with these idealizations, the analytic solution of a periodic, interacting set of flaws with cracks emanating from their tips requires the special mathematical techniques discussed in Appendix B.) Then, for a given confining pressure, we calculate the common orientation in such a manner as to minimize the critical value of the axial compression (the ultimate strength) required to initiate unstable growth of cracks which have been nucleated at flaws' tips.

This calculation also yields a range for possible values of the overall orientation of the failure plane. Then by assuming a reasonable and simple relation between the spacing and the size of such flaws, we estimate the ultimate strength and a range of possible values of the overall fault plane orientation as functions of the confining pressure. This leads to results which are in good qualitative and quantitative agreement with experimental data.

Figure 10 shows the considered model, consisting of an array of flaws of the common initial length $2c$ and of overall orientation ϕ relative to the maximum axial compression σ_1 . The flaws are spaced along the ϕ orientation at the common distance d . The (common) orientation of each flaw relative to the σ_1 axis is denoted by γ . Each flaw can slip in its own plane, transmitting a shear stress, $\tau_{xy}(x) = \tau_c + \mu|\sigma_y|$; see section 2.1. All calculations are performed with $\mu = 0.4$ and $\tau_c = 0$.

3.2. Effects of Overall, ϕ , and Individual, γ , Orientations of Flaws

We fix the confining stress σ_2 , the flaw spacing d/c , and the flaw orientation γ , and we calculate the out-of-plane crack extension length l/c as a function of the axial compression σ_1 for different values of overall orientation ϕ . The method of

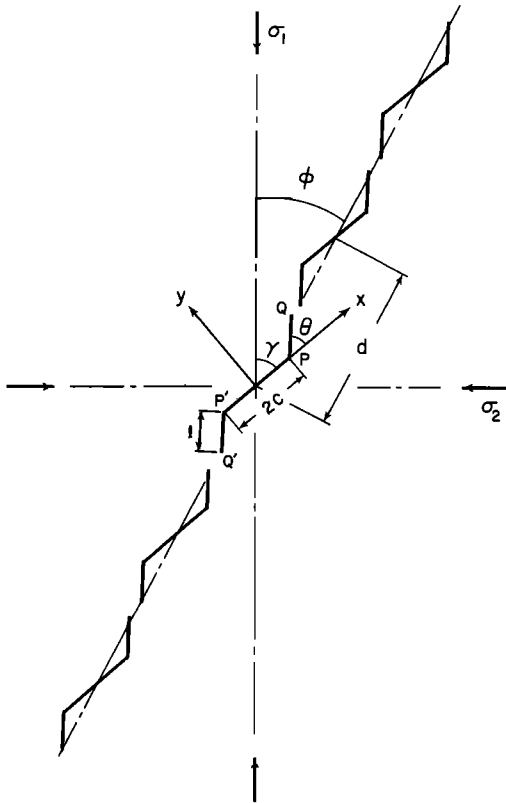


Fig. 10. An unbounded solid with a row of periodically extended preexisting flaws PP' and tension cracks PQ and $P'Q'$.

solution and analytical details are given in Appendix B. Typical results are shown in Figure 11.

In general, for a suitably large value of the overall orientation angle ϕ , the axial compression is a monotonically increasing function of l/c . For the example shown in Figure 11, where $d/c = 4$, $|\sigma_2|(\pi c)^{1/2}/K_c = 0.1$, and $\gamma = 0.24\pi(43^\circ)$, this happens when ϕ exceeds $0.2\pi(36^\circ)$. However, for smaller values of ϕ , the axial compression first increases with increasing l/c , attains a peak value, drops to a minimum value, and then begins to

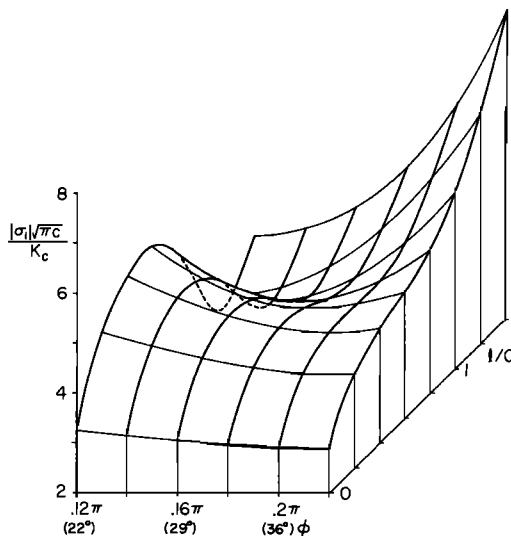


Fig. 11. Variation of axial compression with the crack length and the overall orientation angle; $d/c = 4$, $|\sigma_2|(\pi c)^{1/2}/K_c = 0.1$, $\gamma = 0.24\pi(43^\circ)$, and $\mu = 0.4$.

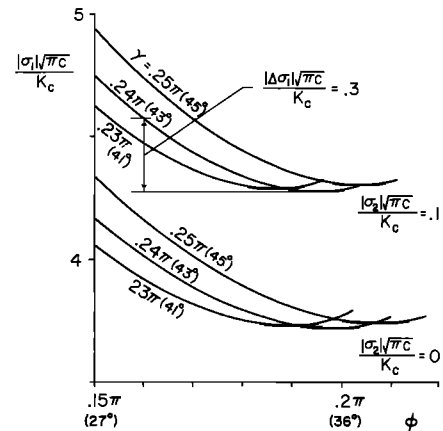


Fig. 12. The peak value of axial compression as a function of overall orientation angle ϕ ; $d/c = 4$, and $\mu = 0.4$.

rise again. This suggests that at a critical value of the axial stress, the growth of cracks emanating from the tips of a set of optimally oriented flaws of this kind can suddenly become unstable, promoting the formation of a macroscopic fault.

To calculate the optimal value for the orientation angle γ , we fix d/c and plot the peak values of σ_1 for each σ_2 and each γ , as functions of ϕ . This is illustrated in Figure 12. We then choose that value of γ which leads to the smallest axial compression for a suitable overall orientation ϕ . This smallest axial compression is defined to be the ultimate strength. In the example of Figure 12, $\gamma = 0.24\pi(43^\circ)$ is the optimal flaw orientation.

Figure 13 shows the axial stress versus crack extension length curves at indicated constant values of the overall orientation ϕ . It is seen that the peak values of the axial stress for the value of ϕ from $0.16\pi(29^\circ)$ to $0.2\pi(36^\circ)$ fall in a very narrow range, i.e., $|\Delta\sigma_1|(\pi c)^{1/2}/K_c \sim 0.3$. This suggests that the presence of inhomogeneities and other imperfections invariably should introduce some uncertainty into the actual orientation of the final fracture plane (a change of about 7° for this example). Indeed, the orientation of fracture planes observed in experiments shows some variations even for similar samples. In the sequel, we shall refer to the quantity $|\Delta\sigma_1|(\pi c)^{1/2}/K_c$ defined above as the "stress barrier."

3.3. Effects of Confining Stress σ_2 and Flaw Spacing d/c

So far, we have shown how to obtain the minimum critical axial stress and the corresponding overall failure orientation

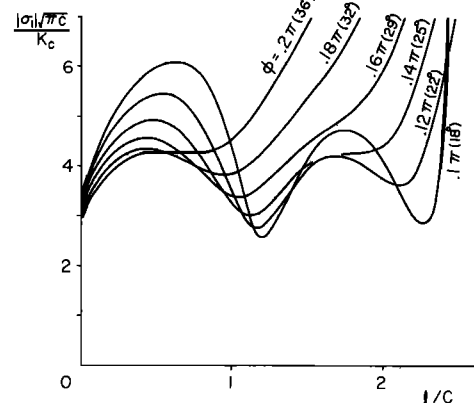


Fig. 13. Axial stress versus crack length for indicated overall orientation; $d/c = 4$, $|\sigma_2|(\pi c)^{1/2}/K_c = 0.1$, $\gamma = 0.24\pi(43^\circ)$, and $\mu = 0.4$.

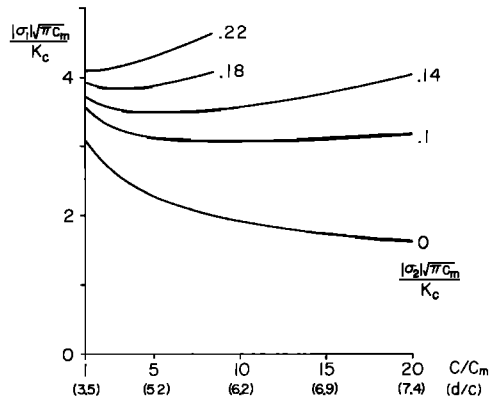


Fig. 14. Ultimate strength, normalized using the minimum flaw size, as a function of flaw size or relative flaw spacing; $\mu = 0.4$.

for fixed values of d/c and σ_2 . We now consider a reasonable relation between the flaw size and its spacing, and we seek to determine the optimal flaw spacing d/c as a function of confining pressure. For an actual sample, we assume that there are many sets of flaws with various d/c , each being "optimal" for a certain confining pressure.

The distribution of d/c depends on the flaw size. Let the minimum flaw size be denoted by c_m and the corresponding flaw spacing by d_m . We assume that smaller flaws are greater in number and closer in spacing than the larger ones. It is then reasonable to regard d/c_m to be a monotonically increasing function of c/c_m . The simplest relation of this kind is

$$\frac{d}{c_m} = b \left(\frac{c}{c_m} \right)^{1+a} \quad b = \frac{d_m}{c_m} \quad a > 0 \quad (1)$$

or, equivalently,

$$\frac{d}{c} = b \left(\frac{c}{c_m} \right)^a \quad (2)$$

In addition, we introduce the largest flaw size c_M , since the size of flaws found in an actual sample is bounded. We then calculate the ultimate strength, $|\sigma_1|(\pi c_m)^{1/2}/K_c$, now normalized using c_m , as a function of d/c or c/c_m for each confining pressure. Typical results are illustrated in Figure 14 for $b = d_m/c_m = 3.5$, $a = 0.25$, and $c_M/c_m = 20$. While these values seem reasonable, their choice has not been guided by any actual observations. Hence, for each confining pressure we can identify the flaw spacing and the flaw size which yield the smallest critical axial stress; this then is regarded to be the ultimate strength for the considered confining pressure. In this manner, we obtain the ultimate strength, the range for the possible values of the fault orientation, and the optimal value of d/c or c/c_m as functions of the confining pressure. Typical results corresponding to Figure 14 are shown in Figures 15a, 15b, and 15c.

The strength-pressure curve is separated into an initial non-linear part and a relatively linear part. By comparing Figures 15a and 15c, it is seen that in the initial nonlinear part the size of active flaws decreases from the maximum c_M to the minimum c_m , and in the linear part, flaws of minimum size are active. As is seen in Figure 15b, the expected fault plane angle ϕ is rather small for small confining pressures, but it increases sharply and stays around 30° at high pressures. In the first part, flaws of maximum size are active. In the second (transition) part the size of active flaws decreases with increasing

lateral pressure, and for the last part, which corresponds to the linear segment of the strength-pressure curve, flaws of minimum size are active. The macroscopic qualitative results of our "model" seem to agree well with experimental observations [Griggs and Handin, 1960; Mogi, 1966].

3.4. Comparison With Experimental Results

As shown above, once parameters which characterize flaw distribution in the model are given, one can estimate the ulti-

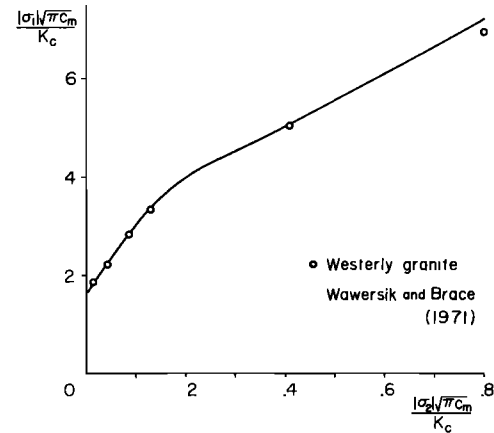


Fig. 15a

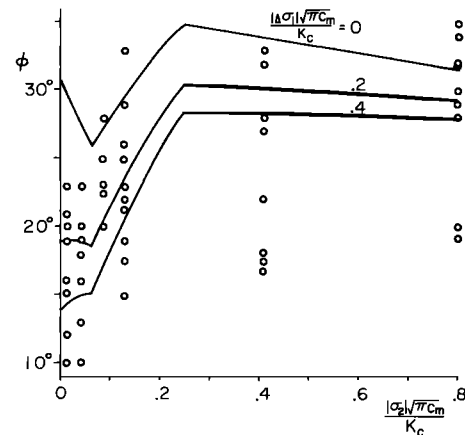


Fig. 15b

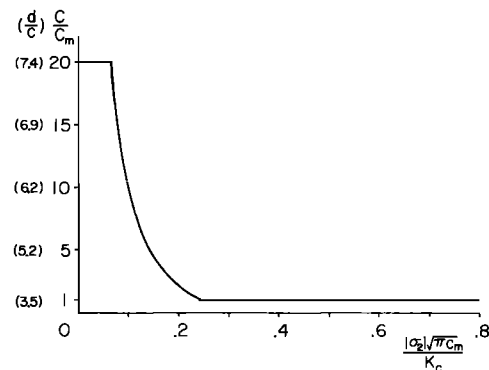


Fig. 15c

Fig. 15. Variation of (a) the ultimate strength, (b) overall failure orientation, and (c) active flaw size or its relative spacing with confining pressure, compared with the experimental data on Westerly granite by Wawersik and Brace [1971].

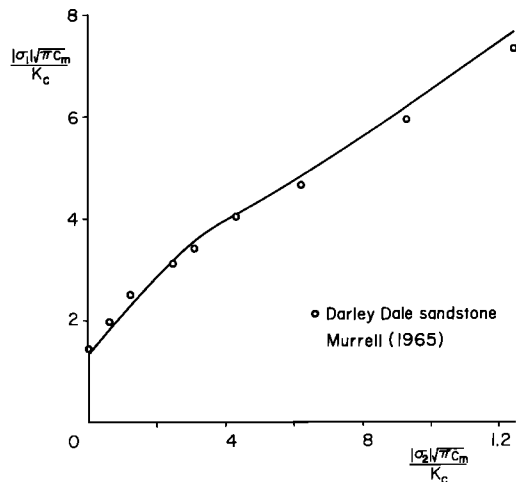


Fig. 16a

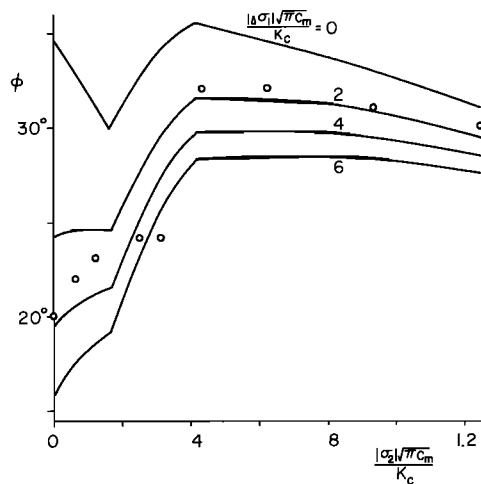


Fig. 16b

Fig. 16. Variation of (a) the ultimate strength and (b) overall failure orientation with confining pressure, compared with the experimental data on Darley Dale sandstone by Murrell [1965].

mate strength and the range for the possible values of the fault orientation as functions of the confining pressure. The parameters for the model may be obtained from the strength-pressure curve observed in actual experiments.

The parameters used to obtain Figures 14 and 15 have been chosen from data on Westerly granite reported by *Wawersik and Brace* [1971]. These data are plotted in Figure 15a, using the normalization factor, $K_c/(\pi c_m)^{1/2} = 27 \times 10^3$ psi (186 MPa). The calculated strength-pressure curve is in good agreement with the experimental data. This, of course, is expected, since the free parameters have been chosen in order to fit the experimental points. The orientation of the overall failure, however, seems to have the right trend, although the experimental data points are scattered over a wide range.

Figures 16a and 16b show a comparison with experimental data on Darley Dale sandstone reported by *Murrell* [1965]. In this case, we have set $d_m/c_m = 3.0$, $a = 0.18$, $c_m/c_m = 10$, and $K_c/(\pi c_m)^{1/2} = 8 \times 10^3$ psi (55 MPa); these choices are not, however, guided by any actual microcrack observations. Both the calculated strength-pressure curve and the orientation of the overall fault plane are in good accord with the observed

data. Note that our theory of shear failure indicates that the orientation of the final failure plane, in general, is different from the orientation of the individual flaws which participate in producing micro-cracks and hence the failure plane.

3.5. Model Experiments: Splitting and Faulting

To accentuate the fundamentally different mechanisms which may be involved in failure by axial splitting and shear failure, we have performed additional model experiments on two specimens with essentially identical, preexisting flaw patterns, one with, and the other without, confinement. These are shown in Figures 17 and 18.

As is seen from Figures 17a and 18a, both specimens contain several large flaws and a number of small equal-sized flaws, which are oriented at 45° relative to the axial compression. The test associated with Figure 17 is done under lateral compression, whereas that associated with Figure 18 is performed without lateral confinement. As discussed in section 2, cracks are nucleated at larger flaws first (Figures 17b and 18b). The cracks are soon arrested for the specimen with confinement, whereas without confinement they continue to grow. Indeed, in the latter case, the cracks extend and join each other, leading to axial splitting (Figure 18c), while no cracks are nucleated at many smaller flaws. The specimen eventually shatters, as shown in Figure 18d, while some small flaws have not even nucleated any cracks. On the other hand, in the presence of confinement, smaller flaws soon become activated, as cracks emanating from larger flaws are arrested because of confining pressure. Then, these smaller flaws interact with each other and nucleate cracks which grow in an unstable manner, leading to a final fault (Figure 17c).

4. SUMMARY AND CONCLUSIONS

1. Micromechanical observations suggest that nucleation, growth, and interaction of microcracks are the dominant, controlling microevents which lead to macroscopic fracture and failure of rocks under overall compression. From the mechanics point of view, any material or geometric discontinuity may produce tension cracks in brittle solids under far-field compression. In an actual specimen there are numerous complex mechanisms which may be responsible for microcracking. The simplest, analytically tractable model of a number of observed microinhomogeneities is a thin flaw which can glide in its own plane, having cohesive, frictional, or both cohesive and frictional resistance, depending on the actual micromechanism that it may be approximating.

2. For such a model flaw, embedded in an elastic solid which is subjected to far-field compressive forces, the exact elasticity boundary value problem is formulated and solved. It is shown that cracks nucleate and grow from the flaw tips and curve toward the direction of maximum compression. If some lateral tension accompanies the axial compression, then the crack growth becomes unstable after a certain crack length is attained. This is considered to be the basic mechanism of axial splitting.

3. The elasticity solution shows that the cracks emanating from the tips of the model flaw are soon arrested if some lateral compression accompanies the axial compression. However, in this case, cracks emanating from the tips of a suitably oriented row of interacting, small model flaws are shown to suddenly grow in an unstable manner, producing a cracked zone. With the aid of model experiments on specimens which contain rows of small flaws and several large flaws, it is shown

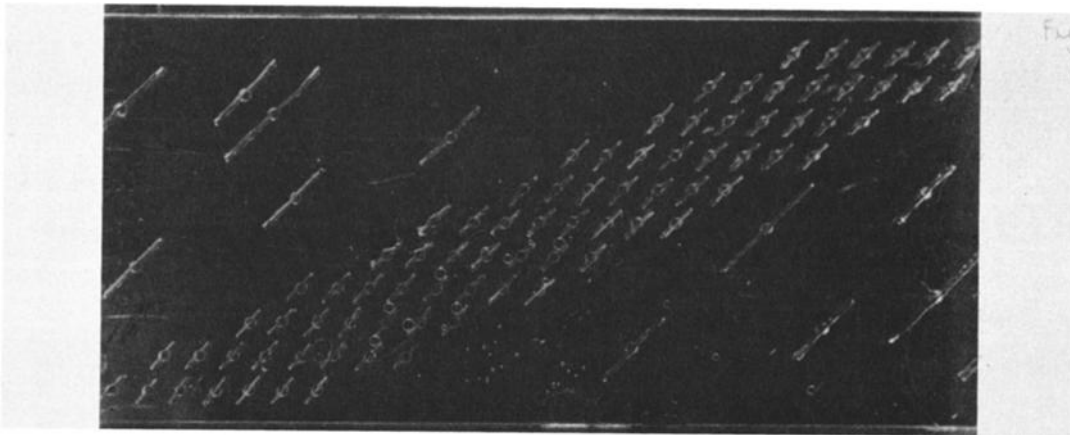


Fig. 17a

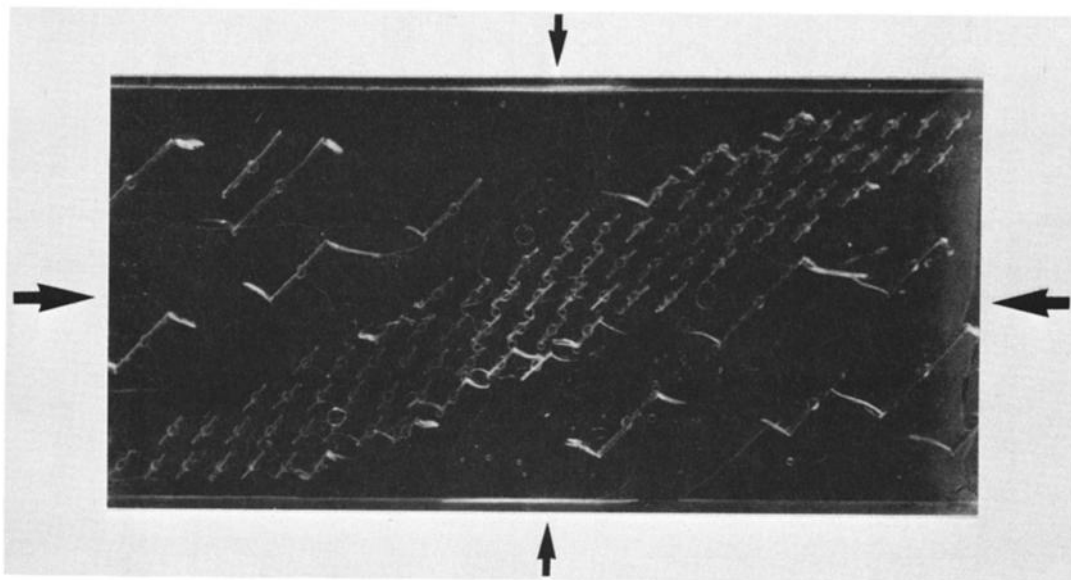


Fig. 17b

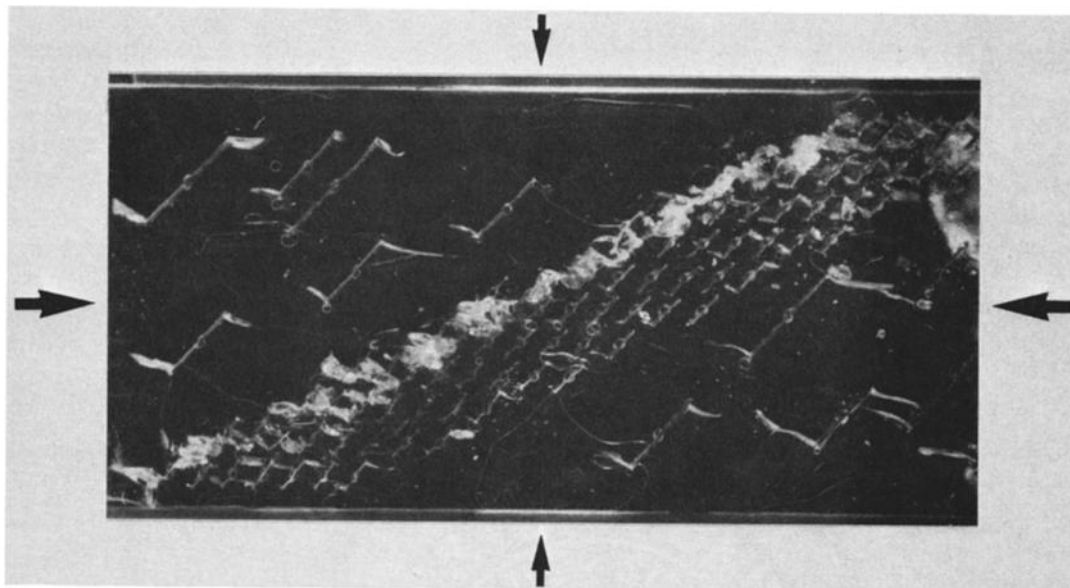


Fig. 17c

Fig. 17. (a) Specimen containing a band of small flaws and several larger flaws. (b) Under axial compression with confinement, tension cracks being nucleated first at larger flaws. (c) Cracks at larger flaws arrested because of confinement and fault formation due to interactive crack growth at smaller flaws.

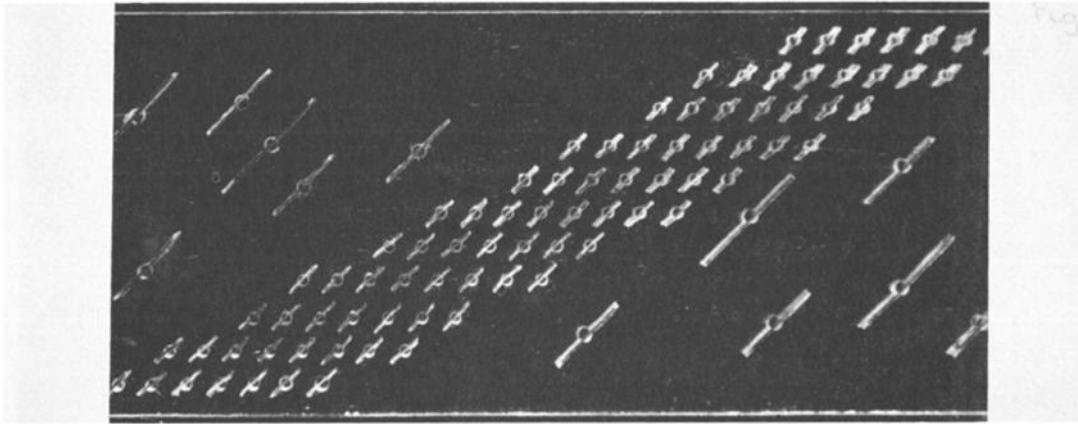


Fig. 18a

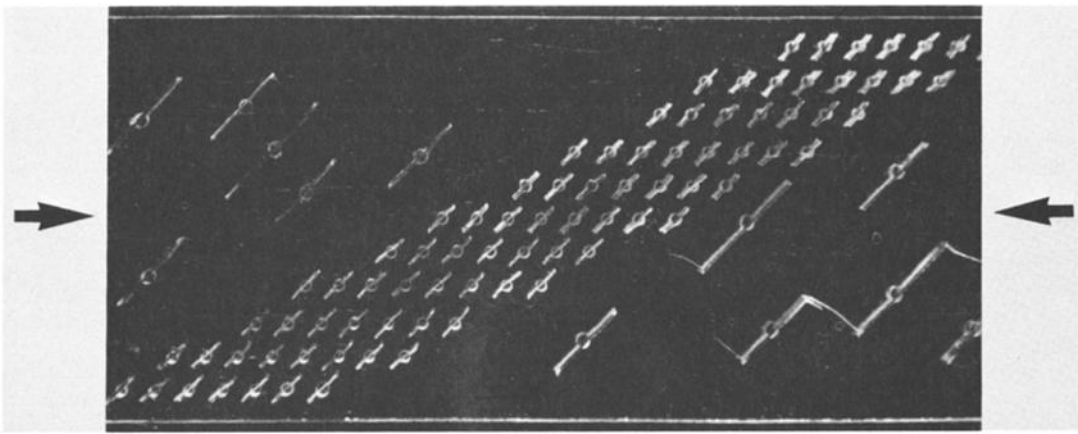


Fig. 18b

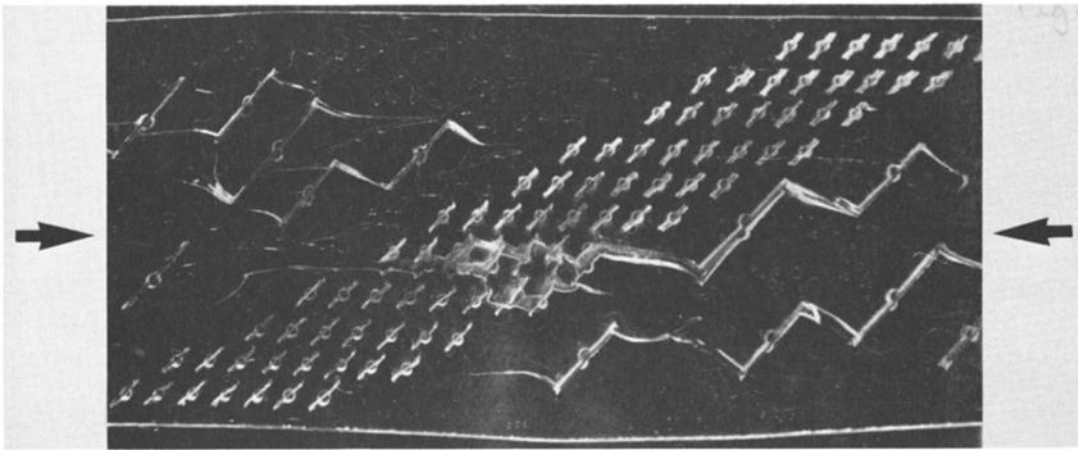


Fig. 18c

Fig. 18. (a) Specimen containing a band of small flaws and several larger flaws (same as in Figure 17a). (b) Under axial compression without confinement, tension cracks being nucleated first at larger flaws. (c) Axial splitting by the growth of cracks at larger flaws. (d) Shattering of specimen while some smaller flaws are still inactive.

that this type of interactive unstable cracking can take place only in the presence of lateral confining pressure: in the absence of lateral confining pressure, only axial splitting is seen to occur. It is suggested that such interactive unstable crack growth may be the basic mechanism which leads to the forma-

tion of a high crack density zone observed in a triaxially compressed rock specimen prior to its apparent shear failure.

4. The proposed model provides a good estimate of the observed ultimate strength and the orientation of the overall failure plane.

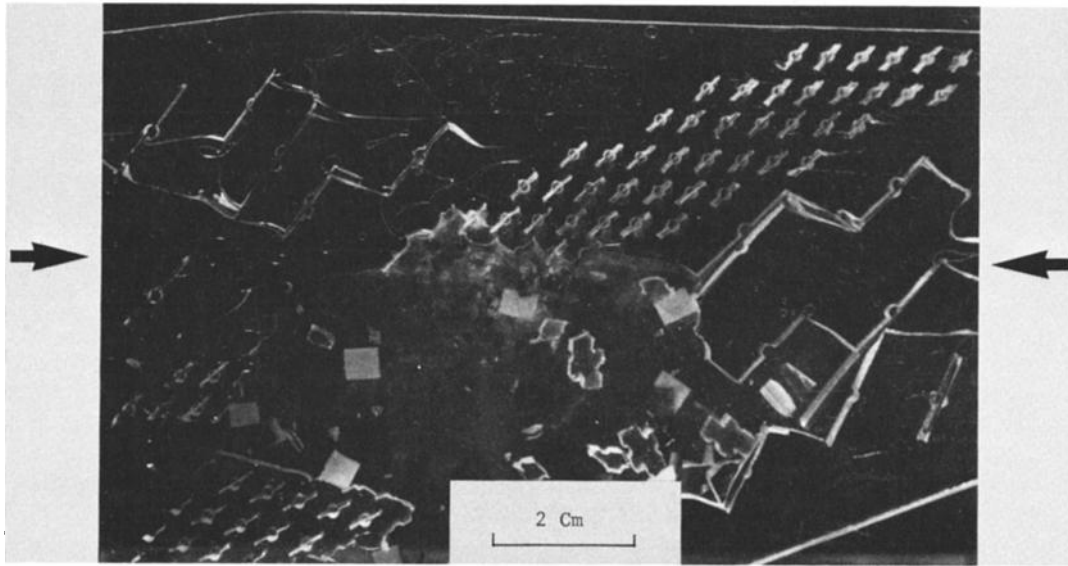


Fig. 18d

Fig. 18. (continued)

APPENDIX A

Consider a two-dimensional (plane strain or plane stress) problem of curved crack extension from the tips of a thin preexisting flaw PP' , under overall compression, as shown in Figure 4. The preexisting flaw PP' of length $2c$ has deformed by slip and frictional sliding under far-field compression, which has resulted in the formation of centrally symmetric tension cracks PQ and $P'Q'$ of equal length l . With respect to the Oxy-coordinate system, let the crack profile be defined by $x = c + g(r)$ and $y = f(r)$, where r measures length along the curved crack. Here σ_1 and σ_2 are the principal stresses at infinity and γ is the angle between the principal σ_1 direction and the x axis. Let σ_x^∞ , σ_y^∞ , and τ_{xy}^∞ denote the components in the Oxy-coordinate system of the far-field stress. We consider the case where $\sigma_1 < 0$, $|\sigma_1| > |\sigma_2|$ and $0 < \gamma < \pi/2$. Then τ_{xy}^∞ is always negative.

It is assumed that the preexisting flaw PP' transmits both cohesive, τ_c , and frictional, $\mu\sigma_y$, shear tractions, where τ_c is the cohesive strength and μ is the friction coefficient (assumed to be a constant) for the flaw material. The boundary conditions on PP' are

$$u_y^+ = u_y^- \quad (A1a)$$

$$\tau_{xy}^+ = \tau_{xy}^- = -\tau_c + \mu\sigma_y \quad (A1b)$$

where the notation is defined in section 2.1. The solutions for a preexisting frictionless, gliding flaw ($\mu = 0$) or a cohesionless frictional flaw ($\tau_c = 0$) are obtained as special cases. Since PQ and $P'Q'$ are tensile cracks, we impose stress free conditions along PQ and $P'Q'$,

$$\sigma_\theta = \tau_{r\theta} = 0 \quad (A2)$$

Following Nemat-Nasser and Horii [1982], we consider Muskhelishvili's [1953] stress functions $\Phi_D = \Phi_0 + \Phi_R$ and $\Psi_D = \Psi_0 + \Psi_R$ for a pair of antisymmetric dislocations at z_0 and $-z_0$ in the complex z plane, which satisfy the following conditions along PP' :

$$\tau_0 + \tau_R = \mu\sigma_0 \quad (A3a)$$

$$\sigma_R = 0 \quad (A3b)$$

where σ_0 and τ_0 , and σ_R and τ_R are the normal and shear

stresses due to Φ_0 and Ψ_0 , and Φ_R and Ψ_R , respectively. In addition, we have the stress functions $\Phi_\infty = \Phi_{\infty 0} + \Phi_{\infty R}$ and $\Psi_\infty = \Psi_{\infty 0} + \Psi_{\infty R}$ for the external forces at infinity, which satisfy the following conditions along PP' :

$$\tau_{xy}^\infty + \tau_{\infty R} = -\tau_c + \mu\sigma_y^\infty \quad (A4a)$$

$$\sigma_{\infty R} = 0 \quad (A4b)$$

where $\sigma_{\infty R}$ and $\tau_{\infty R}$ are the normal and shear stresses due to $\Phi_{\infty R}$ and $\Psi_{\infty R}$, respectively. (Note that (A3b) and (A4b) together with (A10) are sufficient in order to satisfy the continuity condition (A1a).) These stress potentials are defined as follows:

$$\Phi_0 = \alpha \ln \frac{z - z_0}{z + z_0}$$

$$\Psi_0 = \bar{\alpha} \ln \frac{z - z_0}{z + z_0} - \alpha \bar{z}_0 \frac{2z}{z^2 - z_0^2}$$

$$\Phi_R' = (\bar{\alpha}\beta - \alpha\bar{\beta})[F(z, z_0) + F(z, \bar{z}_0)] + (\bar{z}_0 - z_0) \cdot [\alpha\bar{\beta}G(z, z_0) + \bar{\alpha}\beta G(z, \bar{z}_0)]$$

$$\Psi_R' = \bar{\Phi}_R' - \Phi_R' - z\Phi_R'' \quad (A5)$$

$$\Phi_{\infty 0}' = (\sigma_y^\infty + \sigma_x^\infty)/4$$

$$\Psi_{\infty 0}' = (\sigma_y^\infty - \sigma_x^\infty)/2 + i\tau_{xy}^\infty$$

$$\Phi_{\infty R}' = \frac{1}{2}(\tau_{xy}^\infty - \mu\sigma_y^\infty + \tau_c)i[1 - z/(z^2 - c^2)^{1/2}]$$

$$\Psi_{\infty R}' = \frac{1}{2}(\tau_{xy}^\infty - \mu\sigma_y^\infty + \tau_c)i[-zc^2/(z^2 - c^2)^{3/2} + 2z/(z^2 - c^2)^{1/2} - 2]$$

with

$$F(z, z_0) = \left[1 - \frac{z}{z_0} \frac{(z_0^2 - c^2)^{1/2}}{(z^2 - c^2)^{1/2}} \right] \frac{z_0}{z^2 - z_0^2} \quad (A6)$$

$$G(z, z_0) = \frac{\partial}{\partial z_0} F(z, z_0) = \left[1 - \frac{z}{z_0} \frac{(z_0^2 - c^2)^{1/2}}{(z^2 - c^2)^{1/2}} \right] \frac{2z_0^2}{(z^2 - z_0^2)^2} + \left[1 - \frac{zz_0}{(z_0^2 - c^2)^{1/2}(z^2 - c^2)^{1/2}} \right] \frac{1}{(z^2 - z_0^2)}$$

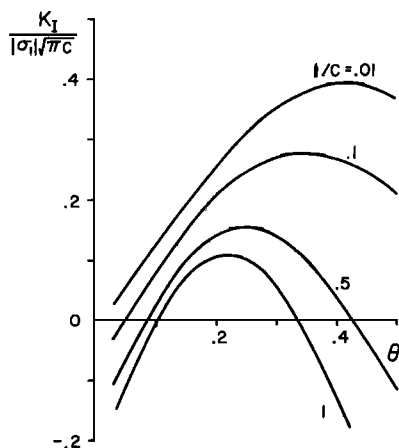


Fig. A1a

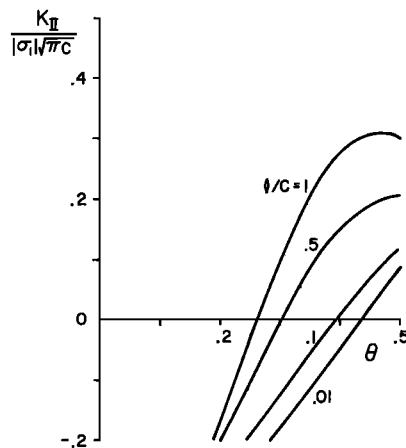


Fig. A1b

Fig. A1. Stress intensity factors at the tip Q of the straight crack, as functions of the crack orientation angle for indicated crack length; $\tau_c = 0$, $\mu = 0.3$, $\sigma_2/\sigma_1 = 0$, and $\gamma = 0.2\pi$ (36°).

where $\alpha = G([u_r] + i[u_\theta])e^{i\theta}/\pi i(\kappa + 1)$, $[u] = u^+ - u^-$, $\kappa = 3 - 4\nu$ for plane strain and $\kappa = (3 - \nu)/(1 + \nu)$ for plane stress, G is the shear modulus, ν is the Poisson ratio, $\beta = (1 + i\mu)/2$, $\Phi = \Phi(\bar{z})$, and $i = (-1)^{1/2}$. From (A3) and (A4), it is seen that the stress functions $\Phi = \Phi_D + \Phi_\infty$ and $\Psi = \Psi_D + \Phi_\infty$ automatically satisfy the second condition of (A1). (Note that in equation (8) of Nemat-Nasser and Horii [1982] and in equation (2.9) of Horii and Nemat-Nasser [1982], the term z/z_0 inside the brackets in the expression for $F(z, z_0)$ is missing. The expression for $G(z, z_0)$ must also be corrected accordingly; for detailed calculations, see Nemat-Nasser [1983].) Hence any collection of dislocations of the kind considered above, will automatically satisfy (A1b).

Suitably distributed dislocations of density $\alpha(r)$ are now introduced to represent the curved crack extensions. Since

$$\sigma_\theta + i\tau_{r\theta} = \Phi' + \overline{\Phi'} + e^{2i\theta}(\bar{z}\Phi'' + \Psi') \quad (\text{A7})$$

it follows from (A2) that

$$\int_0^i [\Phi_D' + \overline{\Phi_D'} + e^{2i\theta}(\bar{z}\Phi_D'' + \Psi_D')] dr + \Phi_\infty' + \overline{\Phi_\infty'} + e^{2i\theta}(\bar{z}\Phi_\infty'' + \Psi_\infty') = 0 \quad (\text{A8})$$

with

$$\begin{aligned} z_0 &= c + g(r) + if(r) & z &= c + g(s) + if(s) \\ \alpha &= \alpha(r) & \theta &= \tan^{-1} [f'(s)/g'(s)] \end{aligned} \quad (\text{A9})$$

The first condition of (A1) requires

$$\int_0^i [\alpha(r) + \bar{\alpha}(r)] dr = 0 \quad (\text{A10})$$

Equation (A8) can be rewritten as

$$\int_0^i \frac{\alpha M_1 + \bar{\alpha} M_2}{s - r} dr + \int_0^i [\alpha L_1 + \bar{\alpha} L_2] dr + (\tau_{xy}^\infty - \mu\sigma_y^\infty + \tau_c)S + \sigma_\theta^\infty + i\tau_{r\theta}^\infty = 0 \quad (\text{A11})$$

where

$$M_1(r, s) = 1/h - e^{2i\theta}\bar{h}/h^2 \quad M_2(r, s) = 1/\bar{h} + e^{2i\theta}/h$$

$$h(r, s) = [g(s) - g(r) + i(f(s) - f(r))]/(s - r)$$

$$L_1(r, z, \theta) = \beta U\{F(z, z_0) + F(z, \bar{z}_0)\}$$

$$+ \beta U\{(z_0 - \bar{z}_0)G(z, z_0)\} - \frac{1}{z + z_0} + e^{2i\theta} \frac{\bar{z} + \bar{z}_0}{(z + z_0)^2}$$

$$L_2(r, z, \theta) = -\beta U\{F(z, z_0) + F(z, \bar{z}_0)\} \quad (\text{A12})$$

$$- \beta U\{(\bar{z}_0 - z_0)G(z, \bar{z}_0)\} - \frac{1}{\bar{z} + \bar{z}_0} + e^{2i\theta} \frac{1}{z + z_0}$$

$$U\{F(z, z_0)\} = U\{\theta; F(z, z_0)\} = -F(z, z_0) + F(\bar{z}, z_0)$$

$$+ e^{2i\theta}[2F(z, z_0) + (z - \bar{z})F'(z, z_0)]$$

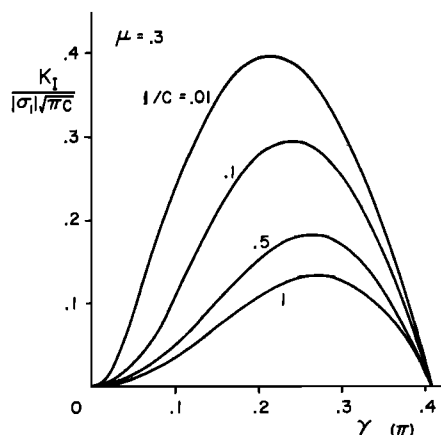


Fig. A2a

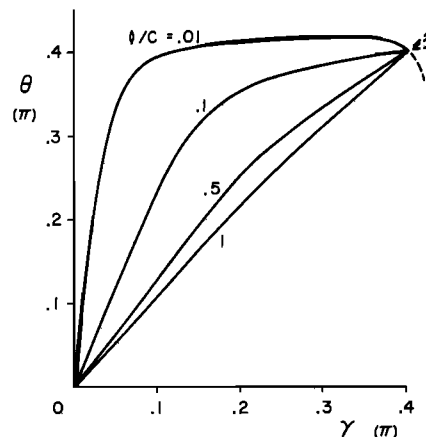


Fig. A2b

Fig. A2. (a) Maximum opening mode stress intensity factors and (b) optimal crack orientation angle as functions of initial flaw orientation; $\tau_c = 0$ and $\sigma_2/\sigma_1 = 0$.

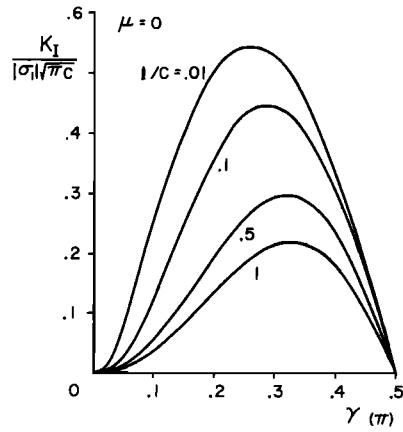


Fig. A3a

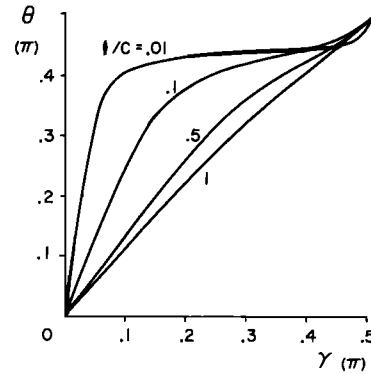


Fig. A3b

Fig. A3. (a) Maximum opening mode stress intensity factors and (b) optimal crack orientation angle as functions of initial flaw orientation; $\tau_c = 0$ and $\sigma_2/\sigma_1 = 0$.

$$S(z, \theta) = \frac{1}{2}i \left\{ \frac{\bar{z}}{(z^2 - c^2)^{1/2}} - \frac{z}{(z^2 - c^2)^{1/2}} + e^{2i\theta} \left[\frac{(\bar{z} - z)c^2}{(z^2 - z_0^2)^{3/2}} + \frac{2z}{(z^2 - c^2)^{1/2}} - 2 \right] \right\}$$

$$\sigma_\theta^\infty + i\tau_{\theta\theta}^\infty = \Phi_{\infty 0}' + \overline{\Phi_{\infty 0}'} + e^{2i\theta}(z\Phi_{\infty 0}'' + \Psi_{\infty 0}')$$

with $z = z(s)$, $z_0 = z_0(r)$ and $\theta = \theta(s)$ given by (A9). Equations (A11) with (A10) form a singular integral equation for the dislocation density α . Solving this integral equation, we obtain the stress intensity factors at the tips of the curved cracks PQ and P'Q', i.e., at points Q and Q', from

$$K_I + iK_{II} = \lim_{r \rightarrow l} \frac{1}{2}(2\pi)^{3/2}(l - r)^{1/2} \cdot [\alpha(r)M_1(r, l) + \bar{\alpha}(r)M_2(r, l)] \quad (A13)$$

For straight crack extensions we have

$$M_1 = 0 \quad M_2 = 2e^{2i\theta} \quad \theta(s) = \theta = \text{constant} \quad (A14)$$

$$z = c + se^{i\theta} \quad z_0 = c + re^{i\theta}$$

For the straight crack extension the above formulation becomes identical with that of Nemat-Nasser and Horii [1982]

except for $F(z, z_0)$ and $G(z, z_0)$, which are corrected according to (A6). This correction alters the numerical results of Nemat-Nasser and Horii [1982] somewhat for large values of l/c , and the new results are given in Figures A1–A5.

For the curved crack extensions, with given crack profile, $f(r)$ and $g(r)$, the singular integral equation (A11) with (A10) is solved numerically using a method suggested by Gerasoulis [1982], and the stress intensity factors are obtained through (A16). The crack profile, defined by $f(r)$ and $g(r)$, is obtained by an incremental procedure where we consider a sequence of incremental straight extensions, each with an orientation which maximizes the opening mode stress intensity factor K_I at the extended crack tip. Typical results of curved extension are shown in Figures 6 and 7 and are discussed in section 2.

Nemat-Nasser and Horii [1982] suggest an approximate scheme for calculating the crack profile, on the basis of the results of straight crack extension calculations; see their equations (21) and the corresponding discussion. Figure 6 compares the calculated crack extension profile for the approximate solution and the complete curved crack extension solution; for additional comparative results [see Horii and Nemat-Nasser, 1983]. It is seen that the straight crack extension model is in good qualitative accord with the more complete

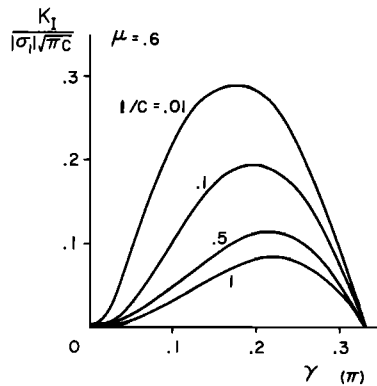


Fig. A4a

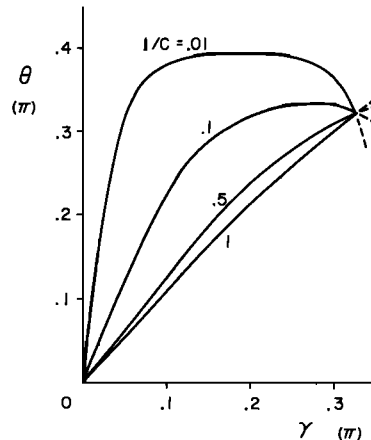


Fig. A4b

Fig. A4. (a) Maximum opening mode stress intensity factors and (b) optimal crack orientation angle as functions of initial flaw orientation; $\tau_c = 0$ and $\sigma_2/\sigma_1 = 0$.

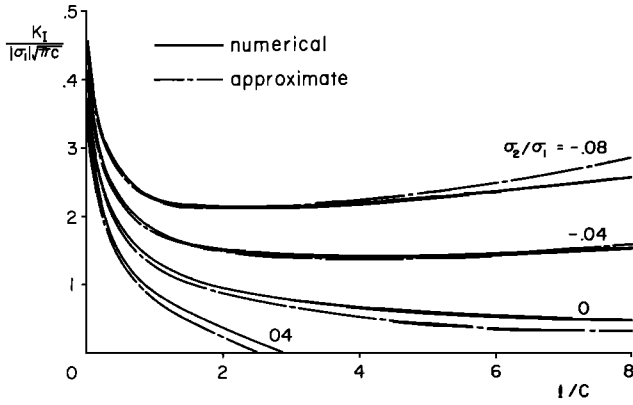


Fig. A5. Variation of maximum stress intensity factor of opening mode with the crack length for indicated σ_2/σ_1 ; $\tau_c = 0$ and $\mu = 0.3$.

curved crack extension solution. Therefore for the sake of simplicity in calculation the straight crack extension model will be used in the sequel and in Appendix B.

As will be seen in Appendix B, the method of pseudo-tractions requires an explicit solution of the singular integral equation (A8). This integral equation can, of course, be solved as accurately as desired, in the manner discussed by *Nemat-Nasser and Horii* [1982]. However, for application to unstable growth of cracks, emanating from the tips of a row of preexisting flaws, the stress intensity factor and other parameters must be calculated repeatedly for a range of values of confining pressure, individual flaw orientation, and other relevant parameters. To simplify this procedure, we introduce an approximate method for the solution of the singular integral equation (A8), which seems to yield results adequately accurate for our numerical estimates.

To this end we assume the following form for the distribution of dislocation density:

$$\alpha(r) = \frac{1}{[r(l-r)]^{1/2}} [\eta^R(2r/l - 1) + i\eta^I r/l] \quad (\text{A15})$$

which satisfies (A10), where η^R and η^I are two real unknown parameters to be determined. Furthermore, we approximate the integrand of the second term in (A11) as

$$\begin{aligned} \alpha(r)L_1(r, z, \theta) + \bar{\alpha}(r)L_2(r, z, \theta) \\ = \frac{1}{[r(l-r)]^{1/2}} \{[(\eta^R + i\eta^I)L_1(l, z, \theta) \\ + (\eta^R - i\eta^I)L_2(l, z, \theta)]r/l \\ - \eta^I[L_1(0, z, \theta) + L_2(0, z, \theta)](1 - r/l)\} \end{aligned} \quad (\text{A16})$$

Making use of (A15) and (A16), (A11) becomes

$$\begin{bmatrix} A_1 & A_2 \\ A_3 & A_4 \end{bmatrix} \begin{bmatrix} \eta^R \\ \eta^I \end{bmatrix} = \begin{bmatrix} (\tau_{xy}^\infty - \mu\sigma_y^\infty + \tau_c) \operatorname{Re}[S] + \sigma_\theta^\infty \\ (\tau_{xy}^\infty - \mu\sigma_y^\infty + \tau_c) \operatorname{Im}[S] + \tau_{r\theta}^\infty \end{bmatrix} \quad (\text{A17})$$

where

$$\begin{aligned} A_1 + iA_3 = \frac{\pi}{2} \left[\frac{8}{l} e^{i\theta} - L_1(l, z, \theta) - L_2(l, z, \theta) \right. \\ \left. + L_1(0, z, \theta) + L_2(0, z, \theta) \right] \\ - A_4 + iA_2 = \frac{\pi}{2} \left[\frac{4}{l} e^{i\theta} + L_1(l, z, \theta) + L_2(l, z, \theta) \right] \end{aligned} \quad (\text{A18})$$

Since s may be suitably chosen, we consider, for convenience, the following expressions:

$$\begin{aligned} s/l &= -0.075(l/c) + 0.475, & l/c < 1 \\ s/l &= -0.0074(l/c)^3 + 0.0156(l/c)^2 \\ &\quad - 0.104(l/c) + 0.489 & 1 < l/c < 4 \\ s/l &= -0.015(l/c) + 0.335 & 4 < l/c \end{aligned} \quad (\text{A19})$$

From (A13), (A17), and (A18) we have

$$K_I + iK_{II} = (2\pi)^{3/2} e^{i\theta} (\eta^R - i\eta^I)/l^{1/2} \quad (\text{A20})$$

Equations (A17) can be solved easily for η^R and η^I and the stress intensity factors at the tips of straight crack extensions are obtained from (A20). Adopting the fracture criterion that the most favorable orientation of the crack extension results in the maximum value of K_I , we calculate the crack orientation angle θ .

The results of the approximate solution are compared with the numerical solutions in Figure A5. It is seen that the drastic approximation shown above yields results with relatively good accuracy.

APPENDIX B

Consider an unbounded solid with a row of periodically distributed preexisting straight thin flaws which have nucleated out-of-plane cracks, as a result of applied far-field compressive forces. The preexisting flaws are of equal size, $2c$, are equally spaced along the ϕ orientation at a distance d , and have a common orientation γ with respect to the σ_1 direction (see Figure 10). The cracks, emanating from the flaws, are assumed to be straight with equal length l and the same orientation θ measured from the common orientation of the preexisting flaws.

The boundary conditions (A1) are assumed to hold on all preexisting flaws, and along the corresponding cracks, the stress-free conditions (A2) are applied.

The problem is solved by making use of the method of pseudo-tractions [*Horii and Nemat-Nasser*, 1983], which is the method for solving the problem of an infinite solid containing interacting microinhomogeneities such as cracks or holes. The solution to the original problem is obtained by the superposition of the solutions of a number of subproblems and of the solution of the problem of an infinitely extended homogeneous solid under applied far-field stresses; for our present problem this is shown in Figure B1. Each subproblem involves an infinite homogeneous solid containing only one of the flaws and its associated cracks. For each subproblem the boundary conditions along the typical preexisting flaw PP' are

$$u_y^+ = u_y^- \quad \tau_{xy} + \tau_{xy}^P + \tau_{xy}^\infty = -\tau_c + \mu(\sigma_y + \sigma_y^P + \sigma_y^\infty) \quad (\text{B1})$$

and along the corresponding cracks PQ and P'Q',

$$\sigma_\theta + \sigma_\theta^P + \sigma_\theta^\infty = 0 \quad \tau_{r\theta} + \tau_{r\theta}^P + \tau_{r\theta}^\infty = 0 \quad (\text{B2})$$

In the sequel, we shall refer to the typical flaw PP' and its associated cracks, PQ and P'Q', collectively as inhomogeneity QQ'. The quantities σ_y^P , τ_{xy}^P , σ_θ^P , and $\tau_{r\theta}^P$ are called the "pseudo-tractions." They are the unknown functions which must be determined in such a manner as to satisfy all boundary conditions of the original problem. The requirement that

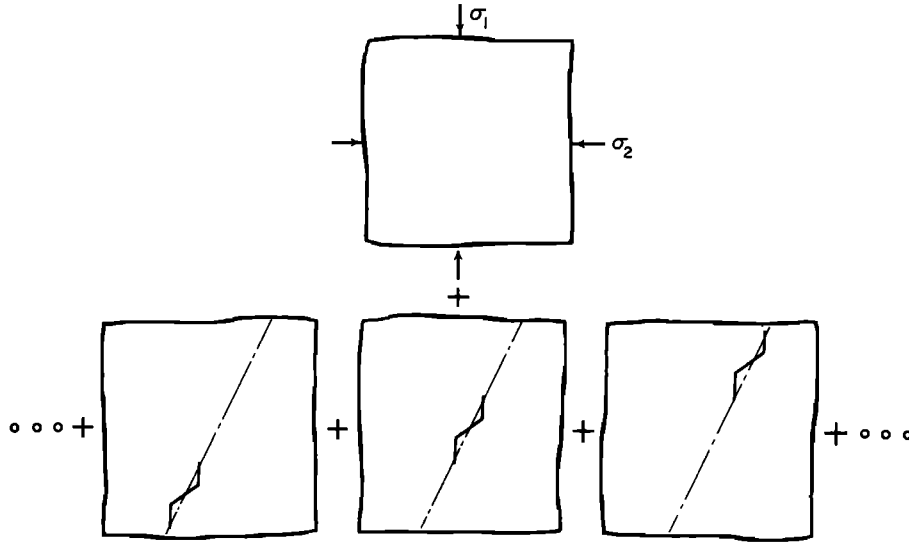


Fig. B1. Decomposition of an original problem into a homogeneous problem and subproblems.

the sum of the subproblems must be equivalent to the original problem leads to a system of integral equations for these pseudo-tractions. These are the "consistency conditions." By discretizing the unknown pseudo-tractions, the system of integral equations is reduced to a system of algebraic equations. Because of symmetry, the pseudo-tractions are the same for all inhomogeneities. For simplicity, we approximate the pseudo-tractions by piecewise constant functions, i.e., we assume that σ_y^P and τ_{xy}^P are constants along PP' and σ_θ^P and $\tau_{r\theta}^P$ are constants along PQ and P'Q'.

Following the approximate method proposed in Appendix A, the solution of a typical subproblem is given by

$$\begin{bmatrix} A_1 & A_2 \\ A_3 & A_4 \end{bmatrix} \begin{bmatrix} \eta^R \\ \eta^I \end{bmatrix} = \begin{bmatrix} [\tau_{xy}^\infty + \tau_{xy}^P - \mu(\sigma_y^\infty + \sigma_y^P) + \tau_c] \operatorname{Re}[S] + \sigma_\theta^\infty + \sigma_\theta^P \\ [\tau_{xy}^\infty + \tau_{xy}^P - \mu(\sigma_y^\infty + \sigma_y^P) + \tau_c] \operatorname{Im}[S] + \tau_{r\theta}^\infty + \tau_{r\theta}^P \end{bmatrix} \quad (\text{B3})$$

where S is given in (A12), and A are given in (A18).

The normal and shear tractions σ_ψ and $\tau_{\rho\psi}$, acting at a point z on a plane inclined from the x direction by the angle ψ , are given by

$$\sigma_\psi + i\tau_{\rho\psi} = B_1(z, \psi)\eta^R + B_2(z, \psi)\eta^I + [\tau_{xy}^\infty + \tau_{xy}^P - \mu(\sigma_y^\infty + \sigma_y^P) + \tau_c]S(z, \psi) \quad (\text{B4})$$

where

$$\begin{aligned} B_1(z, \psi) &= 2 \operatorname{Re} [2I_1 - I_2] + e^{2i\psi}(2I_1 - I_2 + 2II_1 - II_2) \\ &\quad + \frac{\pi}{2} [L_1(l, z, \psi) + L_2(l, z, \psi) - L_1(0, z, \psi) - L_2(0, z, \psi)] \\ B_2(z, \psi) &= -2 \operatorname{Im} [I_1] + ie^{2i\psi}(-I_1 + II_1) \\ &\quad + i \frac{\pi}{2} [L_1(l, z, \psi) - L_2(l, z, \psi)] \end{aligned} \quad (\text{B5})$$

with

$$\begin{aligned} I_1 &= \frac{1}{l} \int_0^l \frac{r \, dr}{[r(l-r)]^{1/2}(z-c-re^{i\theta})} = \frac{e^{-i\theta}}{l} \pi \left\{ \frac{z-c}{[(z-c)(z-z_t)]^{1/2}} - 1 \right\} \\ I_2 &= \int_0^l \frac{dr}{[r(l-r)]^{1/2}(z-c-re^{i\theta})} = \frac{\pi}{[(z-c)(z-z_t)]^{1/2}} \\ II_1 &= -\frac{1}{l} \int_0^l \frac{r(\bar{z}-c-re^{-i\theta}) \, dr}{[r(l-r)]^{1/2}(z-c-re^{i\theta})^2} = -\frac{e^{-3i\theta}}{l} \\ &\quad \cdot \pi \left\{ \frac{(z-c)[(z-c)(3z-3z_t-z+c) + (\bar{z}-c)(z_t-c)e^{2i\theta}]}{2[(z-c)(z-z_t)]^{3/2}} \right\} \\ II_2 &= -\int_0^l \frac{(\bar{z}-c-re^{-i\theta}) \, dr}{[r(l-r)]^{1/2}(z-c-re^{i\theta})^2} \\ &= \frac{e^{-2i\theta}}{l} \frac{(z-c)(z_t-c) - (\bar{z}-c)(z-c+z-z_t)e^{2i\theta}}{2[(z-c)(z-z_t)]^{3/2}} \end{aligned} \quad (\text{B6})$$

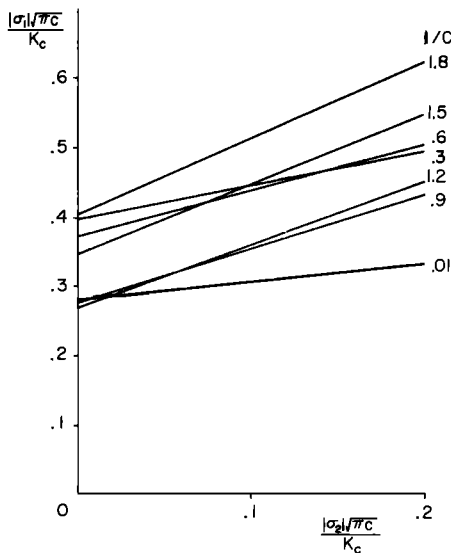


Fig. B2. Axial compressive force as a function of confining pressure for indicated crack length.

Then the "consistency conditions" lead to

$$\sigma_y^P + i\tau_{xy}^P = C_1^c \eta^R + C_2^c \eta^I + [\tau_{xy}^\infty + \tau_{xy}^P - \mu(\sigma_y^\infty + \sigma_y^P) + \tau_c] F^c \quad (B7)$$

$$\sigma_\theta^P + i\tau_{r\theta}^P = C_1^e \eta^R + C_2^e \eta^I + [\tau_{xy}^\infty + \tau_{xy}^P - \mu(\sigma_y^\infty + \sigma_y^P) + \tau_c] F^e$$

where

$$\begin{aligned} C_j^c &= \frac{2}{N} \sum_{n=1}^N B_j(z_{1n}^c, 0) + 2 \sum_{m=2}^{\infty} B_j(z_m, 0) \\ C_j^e &= \frac{1}{N} \sum_{n=1}^N [B_j(z_{1n}^r, \theta) + B_j(z_{1n}^l, \theta)] + 2 \sum_{m=2}^{\infty} B_j(z_m, \theta) \\ F^c &= \frac{2}{N} \sum_{n=1}^N S(z_{1n}^c, 0) + 2 \sum_{m=2}^{\infty} S(z_m, 0) \\ F^e &= \frac{1}{N} \sum_{n=1}^N [S(z_{1n}^r, \theta) + S(z_{1n}^l, \theta)] + 2 \sum_{m=2}^{\infty} S(z_m, \theta) \end{aligned} \quad (B8)$$

with

$$\begin{aligned} z_{1n}^c &= de^{i(\phi-\gamma)} - c + 2c(n-1)/(N-1) \quad z_m = mde^{i(\phi-\gamma)} \\ z_{1n}^r &= de^{i(\phi-\gamma)} + c + le^{i\theta}(n-1)/(N-1) \\ z_{1n}^l &= de^{i(\phi-\gamma)} - c - le^{i\theta}(n-1)/(N-1) \end{aligned} \quad (B9)$$

In equations (B7), the first term in the right-hand side of each equation corresponds to the tractions on one particular inhomogeneity, produced because of the presence of the adjacent inhomogeneities, and the second term corresponds to those produced by all other inhomogeneities. The second term in (B7) can be expanded in even powers of c/md and, in this manner, each series can be summed. In the calculations, N is taken to be 10, and terms of order higher than $(c/d)^{10}$ are neglected.

For given values of d/c , γ , ϕ , σ_2/σ_1 , l/c , and θ , the system of algebraic equations (B3) and (B7) is solved for η^R , η^I , σ_y^P , τ_{xy}^P , σ_θ^P , and $\tau_{r\theta}^P$. Then the stress intensity factors at the tips of the extended cracks are obtained from (A20). The crack orientation angle θ is determined such that the opening mode stress intensity factor K_I is maximized. Setting the value of K_I equal to the fracture toughness K_{IC} , we obtain the required axial compression σ_1 for a given crack extension length l/c .

For fixed values of d/c , γ , and ϕ , we calculate the axial compression σ_1 for each crack extension length l/c , and for different values of σ_2/σ_1 . It turns out that the plot of σ_1 as a function of σ_2 for each l/c , is a straight line. Typical results are shown in Figure B2 for $d/c = 4$, $\gamma = 0.24\pi$ (43°) and $\phi = 0.16\pi$ (29°). From results of this kind, we can now calculate various required parameters for a constant confining pressure σ_2 rather than for a constant stress ratio σ_2/σ_1 .

Acknowledgment. This work has been supported by the U.S. Air Force Office of Scientific Research grants AFOSR-80-0017 and AFOSR-84-0004 to Northwestern University.

REFERENCES

- Banichuk, N. V., Determination of the form of a curvilinear crack by small parameter technique (in Russian), *Izv. Akad. Nauk SSSR Mekh. Tverd. Tela*, 7, 130-137, 1970.
- Bombolakis, E. G., Photoelastic study of initial stages of brittle fracture in compression, *Tectonophysics*, 6, 461-473, 1968.
- Brace, W. F., Brittle fracture of rocks, in *State of Stress in the Earth's Crust*, edited by W. R. Judd, pp. 111-174, Elsevier, New York, 1964.
- Brace, W. F., and E. G. Bombolakis, A note on brittle crack growth in compression, *J. Geophys. Res.*, 68, 3709-3713, 1963.
- Brace, W. F., E. Silver, K. Hadley, and C. Goetze, Cracks and pores—A closer look, *Science*, 178, 162-164, 1972.
- Cottrell, B., and J. R. Rice, Slightly curved or kinked cracks, *Int. J. Fract.*, 16, 155-169, 1980.
- Cottrell, A. H., *Dislocations and Plastic Flow in Crystals*, Clarendon, Oxford, 1953.
- Deng Q. and Zhang P., Research on the geometry of shear fracture zones, *J. Geophys. Res.*, 89, 5699-5710, 1984.
- Dengler, L., Microcracks in crystalline rocks, in *Electron Microscopy in Mineralogy* edited by H. R. Wenk, pp. 550-556, Springer-Verlag, New York, 1976.
- Dey, T. N., and C.-Y. Wang, Some mechanisms of microcrack growth and interaction in compressive rock failure, *Int. J. Rock Mech. Min. Sci. Geomech. Abstr.*, 18, 199-209, 1981.
- Dunn, D. E., L. J. LaFountain, and R. E. Jackson, Porosity dependence and mechanism of brittle fracture in sandstones, *J. Geophys. Res.*, 78, 2403-2417, 1973.
- Fairhurst, C., and N. G. W. Cook, The phenomenon of rock splitting parallel to the direction of maximum compression in the neighborhood of a surface, *Proc. Congr. Int. Soc. Rock Mech. 1st*, 1, 687-692, 1966.
- Friedman, M., R. D. Perkins, and S. J. Green, Observation of brittle-deformation features at the maximum stress of Westerly granite and Solenhofen limestone, *Int. J. Rock Mech. Min. Sci.*, 7, 297-306, 1970.
- Gerasoulis, A., The use of piecewise quadratic polynomials for the solution of singular integral equations of Cauchy type, *Comput. Math. Appl.*, 8, 15-22, 1982.
- Gramberg, J., Axial cleavage fracturing, a significant process in mining and geology, *Eng. Geol.*, 1, 31-72, 1965.
- Griggs, D., and J. Handin, Observations on fracture and a hypothesis of earthquakes, *Rock Deformation*, edited by D. Griggs and J. Handin, *Mem. Geol. Soc. Am.*, 79, 347-364, 1960.
- Hallbauer, D. K., H. Wagner, and N. G. W. Cook, Some observations concerning the microscopic and mechanical behavior of quartzite specimens in stiff, triaxial compression tests, *Int. J. Rock Mech. Min. Sci. Geomech. Abstr.*, 10, 713-726, 1973.
- Hayashi, K., and S. Nemat-Nasser, Energy-release rate and crack kinking under combined loading, *J. Appl. Mech.*, 48, 520-524, 1981.
- Hoek, E., and Z. T. Bieniawski, Brittle fracture propagation in rock under compression, *Int. J. Fract. Mech.*, 1, 137-155, 1965.
- Holcomb, D. J., A quantitative model of dilatancy in dry rock and its application to Westerly granite, *J. Geophys. Res.*, 83, 4941-4950, 1978.
- Holzhausen, G. R., Sheet structure in rock and some related problems in rock mechanics, Ph.D. thesis, Stanford Univ., Stanford, Calif., 1978.
- Holzhausen, G. R., and A. M. Johnson, Analyses of longitudinal splitting of uniaxially compressed rock cylinders, *Int. J. Rock Mech. Min. Sci. Geomech. Abstr.*, 16, 163-177, 1979.
- Horii, H., and S. Nemat-Nasser, Curved crack growth in brittle solids under farfield compression, *Advances in Aerospace Structures and Materials*, edited by R. M. Laurenson and U. Yuceoglu, *AD Publ. Am. Soc. Mech. Eng. Aerosp. Div.*, AD 03, 75-81, 1982.
- Horii, H., and S. Nemat-Nasser, Estimate of stress intensity factors for interacting cracks, *Advances in Aerospace Structures, Materials and Dynamics*, edited by U. Yuceoglu, R. L. Sierakowski, and D. A. Glasgow, *AD Publ. Am. Soc. Mech. Eng. Aerosp. Div.*, AD 06, 111-117, 1983.
- Hoshino, K., and H. Koide, Process of deformation of the sedimentary rocks, *Proc. Congr. Int. Soc. Rock Mech. 2nd*, 1, 353-359, 1970.
- Ingraffea, A. R., and F. E. Heuze, Finite element models for rock fracture mechanics, *Int. J. Numer. Anal. Methods Geomech.*, 4, 25-43, 1980.
- Kachanov, M. L., A microcrack model of rock inelasticity, I, Frictional sliding on microcracks, *Mech. Mater.*, 1, 19-27, 1982a.
- Kachanov, M. L., A microcrack model of rock inelasticity, II, Propagation of microcracks, *Mech. Mater.*, 1, 29-41, 1982b.
- Karihaloo, B. L., On crack kinking and curving, *Mech. Mater.*, 1, 189-201, 1982.
- Kranz, R. L., Crack-crack and crack-pore interactions in stressed granite, *Int. J. Rock Mech. Min. Sci. Geomech. Abstr.*, 16, 37-47, 1979.
- Kranz, R. L., Microcracks in rocks: A review, *Tectonophysics*, 100, 449-480, 1983.

- Liu, H. P., and A. C. R. Livanos, Dilatancy and precursory bulging along incipient fracture zones in uniaxially compressed Westerly granite, *J. Geophys. Res.*, **81**, 3495–3510, 1976.
- Lo, K. K., Analysis of branched cracks, *J. Appl. Mech.*, **45**, 797–802, 1978.
- Lockner, D., and J. Byerlee, Acoustic emission and fault formation in rocks, in *Proceedings of 1st Conference on Acoustic Emission/Microseismic Activity in Geologic Structures and Materials*, edited by H. R. Hardy Jr. and F. W. Leighton, pp. 99–107, Trans. Tech Publications, Clausthal-Zellerfeld, Federal Republic of Germany, 1977.
- McClintock, F. A., and J. B. Walsh, Friction on Griffith cracks in rocks under pressure, in *Proceedings of the 4th U.S. National Congress on Applied Mechanics 1962*, vol. 2, pp. 1015–1021, American Society of Mechanical Engineers, New York, 1963.
- Mogi, K., Pressure dependence of rock strength and transition from brittle fracture to ductile flow, *Bull. Earthquake Res. Inst. Tokyo Univ.*, **44**, 215–232, 1966.
- Moss, W. C., and Y. M. Gupta, A constitutive model describing dilatancy and cracking in brittle rocks, *J. Geophys. Res.*, **87**, 2985–2998, 1982.
- Murrell, S. A. F., The effect of triaxial stress systems on the strength of rocks at atmospheric temperatures, *Geophys. J. R. Astron. Soc.*, **10**, 231–281, 1965.
- Muskhelishvili, N. I., *Some Basic Problems in the Mathematical Theory of Elasticity*, Noordhoff, Groningen, Netherlands, 1953.
- Nemat-Nasser, S., On stability of the growth of interacting cracks, and crack kinking and curving in brittle solids, in *Numerical Methods in Fracture Mechanics, Proceedings of Second International Conference*, edited by D. R. J. Owen and A. R. Luxmoore, pp. 687–706, Pineridge Press, Swansea, United Kingdom, 1980.
- Nemat-Nasser, S., Non-coplanar crack growth, in *Proceedings of the ICF International Symposium on Fracture Mechanics*, Science Press, pp. 185–197, Beijing, People's Republic of China, 1983.
- Nemat-Nasser, S., and H. Horii, Compression-induced nonplanar crack extension with application to splitting, exfoliation, and rockburst, *J. Geophys. Res.*, **87**, 6805–6821, 1982.
- Olsson, W. A., and S. S. Peng, Microcrack nucleation in marble, *Int. J. Rock Mech. Min. Sci. Geomech. Abstr.*, **13**, 53–59, 1976.
- Palaniswamy, K., and W. G. Knauss, On the problem of crack extension in brittle solids under general loading, in *Mechanics Today*, vol. 4, edited by S. Nemat-Nasser, pp. 87–148, Pergamon, New York, 1978.
- Paterson, M. S., Experimental deformation and faulting in Wombeyan marble, *Bull. Geol. Soc. Am.*, **69**, 465–476, 1958.
- Paterson, M. S., *Experimental Rock Deformation—The Brittle Field*, Springer-Verlag, 1978.
- Peng, S. D., Stresses within elastic circular cylinders loaded uniaxially and triaxially, *Int. J. Rock Mech. Min. Sci.*, **8**, 399–432, 1971.
- Peng, S. S., and A. M. Johnson, Crack growth and faulting in cylindrical specimens of Chelmsford granite, *Int. J. Rock Mech. Min. Sci.*, **9**, 37–86, 1972.
- Pollard, D. D., P. Segall, and P. T. Delaney, Formation and interpretation of dilatant echelon cracks, *Bull. Geol. Soc. Am.*, **93**, 1291–1303, 1982.
- Scholz, C. H., Experimental study of the fracturing process in brittle rock, *J. Geophys. Res.*, **73**, 1447–1454, 1968.
- Segall, P., and D. D. Pollard, Mechanics of discontinuous faults, *J. Geophys. Res.*, **85**, 4337–4350, 1980.
- Soga, N., R. J. Martin III, and H. Spetzler, Inhomogeneous strain accumulation on laboratory rock samples prior to failure (abstract), *Eos Trans. AGU*, **57**, 328, 1976.
- Soga, N., H. Mizutani, H. Spetzler, and R. J. Martin III, The effect of dilatancy on velocity anisotropy in Westerly granite, *J. Geophys. Res.*, **83**, 4451–4458, 1978.
- Sprunt, E. S., and W. F. Brace, Direct observation of microcavities in crystalline rocks, *Int. J. Rock Mech. Min. Sci. Geomech. Abstr.*, **11**, 139–150, 1974.
- Tapponnier, P., and W. F. Brace, Development of stress-induced microcracks in Westerly granite, *Int. J. Rock Mech. Min. Sci. Geomech. Abstr.*, **13**, 103–112, 1976.
- Wawersik, W. R., and W. F. Brace, Post-failure behavior of a granite and diabase, *Rock Mech.*, **3**, 61–85, 1971.
- Wong, T. F., Effects of temperature and pressure on failure and post-failure behavior of Westerly granite, *Mech. Mater.*, **1**, 3–17, 1982a.
- Wong, T. F., Micromechanics of faulting in Westerly granite, *Int. J. Rock Mech. Min. Sci. Geomech. Abstr.*, **19**, 49–64, 1982b.
- Wu, C. H., Elasticity problems of a slender Z-crack, *J. Elasticity*, **8**, 183–205, 1978.

H. Horii and S. Nemat-Nasser, Department of Civil Engineering, The Technological Institute, Northwestern University, Evanston, IL 60201.

(Received April 24, 1984;
revised November 6, 1984;
accepted November 9, 1984.)